Recurrent circuits encode visual center-surround computations in the mouse superior colliculus

Peng Cui[1*], Kuisong Song[2*], Dimitris Mariatos-Metaxas[1], Arturo G. Isla[3,4], Teresa Femenia[2], Iakovos Lazaridis[5], Konstantinos Meletis[1], Arvind Kumar[1,6] and Andreas A. Kardamakis[1,2,#]

[1]*Department of Neuroscience, Karolinska Institute, Stockholm, Sweden*
[2]*Instituto de Neurociencias CSIC-UMH, San Juan de Alicante, Spain*
[3]*Tecnológico de Monterrey, Escuela de Medicina y Ciencias de la Salud, México*
[4]*Department of Neurobiology, Care Sciences and Society, Karolinska Institute, Sweden*
[5]*McGovern Institute, Massachusetts Institute of Technology, Cambridge, USA*
[6]*Division of Computational Science and Technology. School of Electrical Engineering and Computer Science. KTH Royal Institute of Technology, Stockholm, Sweden*
[*] These authors contributed equally to the work
[#]*Corresponding author*

Send correspondence to lead contact:

Andreas Kardamakis
Instituto de Neurociencias CSIC-UMH
Avenida Santiago Ramón y Cajál s/n
San Juan de Alicante, 03015
Spain

Email:
akardamakis@umh.es
andreas.kardamakis@ki.se

Abstract

The interaction of retinal center-surround processes with early visual subcortical and cortical circuits forms the basis for saliency computations. The subcortical circuit mechanisms contributing to surround modulation, however, remain unclear. We developed an optogenetic approach to functionally delineate visual center and surround zones of individual neurons in the superficial layers of the superior colliculus (SCs). We demonstrate that local circuit interactions within the SCs are sufficient to generate surround suppression and that surround network activation leads to decreases in center excitation rather than increases in synaptic inhibition. Using a range of complementary methods, we reveal the identity of a SCs-based circuit with two key interacting circuit motifs, recurrent excitation and feedback inhibition, capable of modulating levels of center excitation when the visual surround is active. We propose that subcortical and cortical visual circuits are both

recurrent-based and have evolved to independently perform surround modulation, thus enabling parallel saliency computations across multiple levels.

Introduction

Enabling neurons to compare central inputs with their immediate surround represents a fundamental and conserved computation [1,2]. Termed 'surround modulation' and usually suppressive, it is widespread across sensory modalities such as vision [3], hearing [4], somatosensation [5], and olfaction [6]. A typical example found across species is during size tuning of a visual neuron; the firing response initially increases when a stimulus is centered on its receptive field [7,8], but then decreases as the stimulus expands beyond this area [9–12]. Such observations have been measured throughout the visual thalamocortical system - in the lateral geniculate nucleus [13], primary visual cortex 'V1' [14] and extrastriate cortex [15] - and retinotectal systems in the premammalian optic tectum [9,16,17] or superior colliculus 'SC' [8,10]. While center-surround interactions are known to originate in the retina, which has been extensively studied [18–21], little is known about the extent to which they are inherited by later stages of the visual hierarchy and how extraretinal circuits in the SC and V1 can actively contribute to surround modulation.

This process relies on the interplay between excitatory cells releasing glutamate and inhibitory cells releasing GABA (γ-aminobutyric acid). As intuition would suggest, surround suppression can be mediated by increases of levels of GABAergic inhibition, however, different neural systems may assume different mechanisms [22]. For example, surround suppression in the primary visual cortex (V1) is driven by decreases in levels of excitation rather than increases in synaptic inhibition [23]. Determining this mechanism, along with its underlying circuit motifs, is essential for uncovering the minimal circuitry underlying surround network interactions. This insight brings us one step closer to interpreting how cortical signals can interact with SC circuitry for saliency computations [24–26] or visuospatial behavior like target selection in overt [27,28] and covert attention [29,30].

Here, we demonstrate that early visual circuits within the superficial layers of the superior colliculus (SCs) contain the sufficient circuitry to generate center-surround interactions in absence from any extrinsic input. To reveal the circuit mechanism, we devised a functional receptive field mapping approach that uses optogenetics and whole-cell electrophysiology to delineate and selectively activate center and surround zones of single neurons. Through this approach, we found that robust surround suppression is mediated by decreases in levels of excitation in absence of any increase in synaptic inhibition. We subsequently identified the underlying functional circuit motifs between local excitatory (*E*) and inhibitory (*I*) neurons using cell-type-specific trans-synaptic mapping. Large-scale computational modelling revealed the minimal circuit connections among those identified motifs, revealing the importance of local recurrent excitatory interactions critical for generating visual surround suppression in the SCs. Finally, we observed functional decreases in the E/I balance in the

surround when the center was active by using *in vivo* cfos induction with optogenetics, thus confirming a key model prediction. In sum, our results suggest that phylogenetically older early visual circuits, based in the SCs, are capable of generating surround suppression independently of cortical saliency computations, while still sharing common circuit strategies in their diverse implementation.

Results

Visual surround network activation modulates center excitability in the SCs

To establish the mechanism and circuit basis of midbrain visual surround modulation, we sought to recapitulate 'classical' center and surround interactions using an *ex vivo* experimental setting by substituting visual stimulus patterns with optogenetically-induced retinotopic impulse patterns in midbrain sections of the SCs (Fig. 1a-c). By leveraging the aligned topographic correspondence of the retinotectal pathway [31], we generated an input-dependent visual field. We made it light-excitable by injecting an adeno-associated virus (AAV) intravitreally that expressed ChR2 in retinal ganglion cells (RGCs) of both wild-type C57BL/6NCrl (n = 22, N = 14) and vGAT-Cre (n = 7, N = 5) mice (*see* top panel, Fig. 1a). To ensure sufficient expression of ChR2 across the SCs, pan-retinal transfection was an essential prerequisite for trial inclusion (Bottom left, Fig. 1a); partial expressions were not taken into consideration to minimize the risk of false positive surround classification that could arise from lack of ChR2 expression. We mapped the receptive fields of single SCs neurons (n = 29, N = 19), referred herein to as center zones (C), by detecting subregions that triggered excitatory postsynaptic currents (EPSCs) in response to site-specific light patterns (Fig. 1b-c), which would activate the retinotopically arranged ChR2-expressing RGC axonal terminals in coronal SC sections (Bottom right, Fig. 1a).

Given the *a priori* unknown perimeter of each neuron's center zone, the surround zone (S) can exhibit significant spatial variability and extend over a wide area (Fig. 1b-c). To accurately cover each neuron's center zone and ensure a significant surround area, it was essential to create a sufficiently large field of view (FOV) that could accommodate their distinct morphologies. To do this, we used one-photon widefield optics via a low magnification objective (16×) while using an in-house built dual-focus visual inspection system to selectively magnify or demagnify the optical path (Fig. 1b). Demagnification (by 0.5×) captured a large field of view of > 1mm^2 that incorporated most of the SCs (magenta box in lower right of Fig. 1a), thus allowing for patterned micro-optostimulation of the entire visual layer. The other path diverted the light for magnification (by 2×), thereby achieving sufficient single cell resolution to visually target our neurons of interest for whole-cell recordings (Fig. 1b). This *functional receptive field mapping* approach allowed us to delineate spatial patterns defining center and surround regions of single neurons, which were subsequently used to selectively activate separately or in sequences during recordings.

Figure 1c illustrates the center zone of a vGAT+ horizontal cell, which was determined by measuring evoked EPSCs after optostimulation (5 impulses at 10 Hz) of a 10 × 10 grid covering the FOV. The areas that evoked EPSC amplitudes exceeding 10-20% of the peak value (*see* Supplementary Fig. S1) collectively formed an image pattern that were classified as the center, which usually encompassed the soma and the majority of the dendritic processes (Bottom left, Fig. 1c; *see* also Supplementary Fig. S1 and S4). Selective activation of this center zone always triggered short-latency compound EPSCs (mean amplitude: 120.8 ± 15.5 pA) characterized by prominent multimodal peaks (*see* arrowheads in the magenta trace in Fig. 1d), suggesting the presence of local recurrent excitatory-excitatory connectivity in addition to monosynaptic excitatory RGC input (Fig. 2-3).

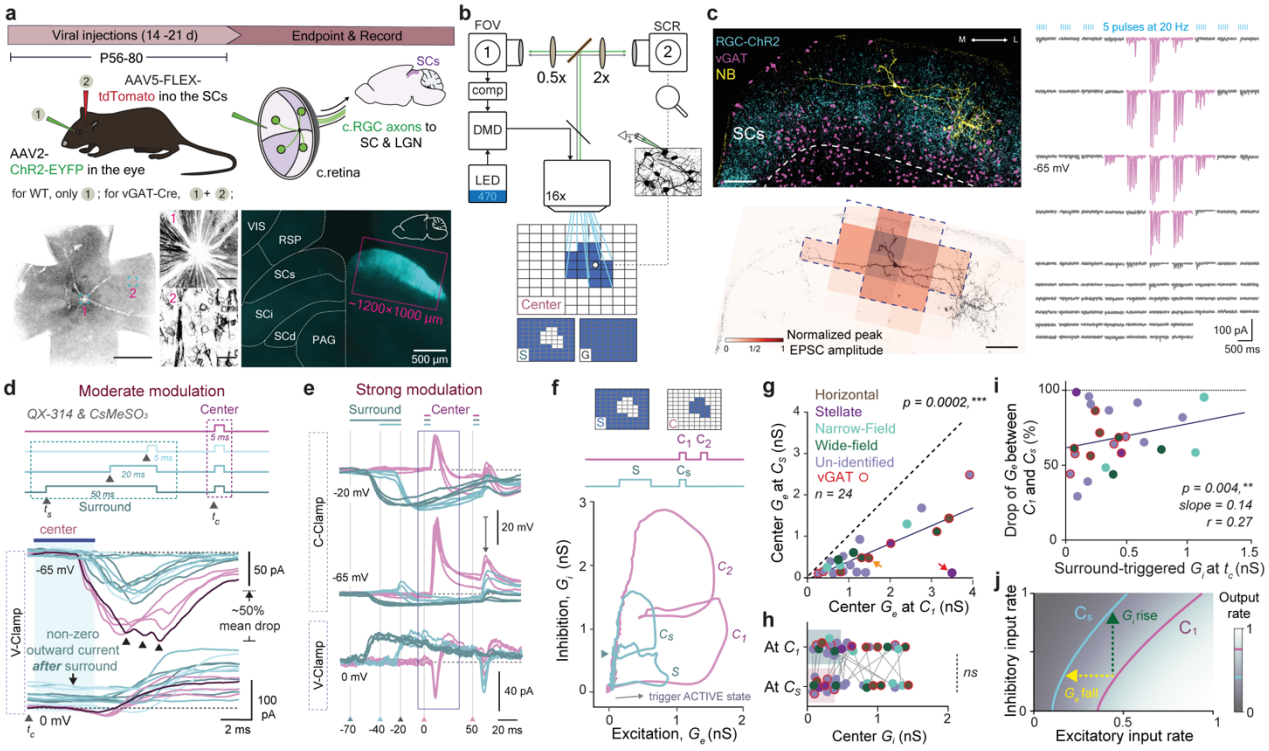

Fig. 1: Visual surround network activation modulates center excitability in SCs cell-types.
(a) Top: Procedure showing expression of ChR2 in RGCs using an intravitreal viral injection of the vector rAAV2-hsyn-hChR2(H134R)-EYFP (in WT mice, *N=14*) and unilateral labeling of contralateral SCs inhibitory neurons with the vector rAAV5-FLEX-tdTomato (in this case vGAT-Cre mice were used, *N=5*). Bottom left: Inverted fluorescent image of whole retinal mount confirming homogeneous transfection of RGCs with ChR2-EYFP. Scale bar: 1200 µm. Insets show enlarged aspects of the optic disc (1) and individual RGCs (2). Scale bar: 25 µm. Bottom right: Coronal midbrain section with ChR2-expressing RGC axonal terminals seen occupying the SCs layers.
(b) A dual magnification setup for functional receptive field mapping of single cells. This enabled the simultaneous visualization of a large field of view (FOV) encompassing the SCs layer, and single cell resolution (SCR) for identifying center excitation zones using whole-cell recordings and patterned optostimulation via a digital mirror device (DMD). *See* also experimental procedures and Fig. S1-S4.
(c) Top left: a representative example of this approach applied to an inhibitory horizontal SCs neuron stained intracellularly with Neurobiotin (NB). Scale bar: 100 µm. The neuron responds with excitatory postsynaptic currents (EPSCs, shown in magenta) to a 20 Hz 5-light-pulse train delivered pseudo-randomly. Each trace comes from a single optostimulated rectangular area of 120×100 µm (shown on the right). Bottom left: reconstructed neuron is shown with the denoted excitation zone (dotted line), which is referred to as center, whereas the non-responsive areas as surround (S) zone. Whole-field optostimulation is referred to as 'global' (G).

(d) Synaptic modulation between the center and surround zone of the neuron shown in (c). Top: Temporal patterns underlying surround and center interaction. Bottom: Individual traces of synaptic inward and outward currents evoked in response to center stimulation when recording at reversal equilibriums for $GABA_A$-chloride mediated inhibition and glutamatergic excitation (-65 and 0 mV, respectively). Arrowheads show EPSC recurrence in an individual trace (darker shade). Scale bar: 100 µm. Full traces in Fig. S2.
(e) Voltage traces revealing the strong modulation that the surround exerts on center activity in a stellate SCs interneuron. Voltage responses during surround followed by center (green traces) at two membrane holding potentials (-20 mV and -65 mV, top and middle, respectively) or during center alone (magenta). Bottom: Current traces when holding at 0 mV using the same condition.
(f) Plot of the inhibitory conductance as a function of the excitatory conductance in the neuron shown in (c) and (d). Arrow shows direction of process when neuron is activated.
(g-h) Comparison of synaptic excitatory and inhibitory conductances between conditions: center only (C_1) and center after surround (C_s). Color coding corresponds to morphologically or genetically identified SCs neuron cell-types. Orange and red arrows depict data points from neurons shown in (d) and (e), respectively.
(i) Modulation of center excitation plotted as a function of inhibitory conductance that is present at the time of center optostimulation (t_c).
(j) Schematic showing how the same level of response suppression can be achieved by either decrease in excitatory conductance or by increase in the inhibitory conductance. The gray colormap indicates a 2D input-output transfer function of a neuron as a function of normalized input excitation and inhibition. The two curved lines indicate iso-firing rate contours.
Statistical comparisons were performed as paired *t*-tests followed by Wilcoxon rank-signed tests. *Abbreviations: c.*, contralateral; *WT*, wild-type; *RGC*, retinal ganglion cell; *VIS,* primary visual cortex; *RSP*, retrosplenial cortex; *SCs*, superior colliculus superficial layer; *SCi*, superior colliculus intermediate layer; *SCd*, superior colliculus deep layer; *PAG*, periaqueductal gray matter.

Optostimulation of the center zone (control traces in magenta) always resulted in an excitatory phase quickly followed by an inhibitory one (Fig. 1d-f). To induce center-surround interactions, we first activated the surround using three different durations and onsets (*see* dotted box in Fig. 1d). Light stimulation intensity was held constant for both the center and surround zones. The surround-stimulation phases were terminated 20 ms before center-stimulation onset to ensure adequate time for the build-up of surround-induced activity while allowing for signal synchronization with the center-induced activity (cyan traces in Fig. 1d; *see* also Fig. S3d). Obviously, within these experimental settings, simultaneous center and surround activation, akin to whole-field (global) stimulation (Fig. 1b and 2i), would mask any discernible effect the surround would have on the center. Comparing the magenta and cyan traces in Fig. 1d reveals a distinct and consistent decline in center responsiveness after surround activity, seen by a significant reduction in center-evoked EPSC amplitudes (~50% decrease in this recorded cell) along with a concurrent decrease in the number of multimodal peaks. In line with previous studies [9,32], these evoked EPSCs were rapidly followed (mean peak latency ± s.e.m.: 5.9 ± 0.8 ms) by a feedforward inhibitory component (mean amplitude ± s.e.m.: 24.3 ± 5.0 pA) observed at the equilibrium potential for glutamate-mediated excitation (0 mV, bottom of Fig. 1d), and here we observe that it occurred regardless of the presence of a preceding surround.

The degree of surround modulation varied across different SCs neurons. Based on the intensity of the reduction in center EPSC amplitude, the suppression was classified as mild, moderate or strong (Fig. 1d-e; strong: > 60%, n = 9/24; moderate: 20-60%, n = 10/24; mild: < 20%, n = 5/24). Figure 1e

195 shows the voltage and current traces of a stellate SCs interneuron that was subject to a strong
196 surround influence (*see* Supplementary Fig. S2 and S4). When its surround was activated first, visual
197 input arriving to the neuron's center zone (top and middle traces) was completely suppressed by an
198 outward current pulling its membrane potential toward the reversal for chloride-mediated $GABA_A$ (γ-
199 aminobutyric acid type A) inhibition (~69 mV; *see* bottom traces in Fig. 1e). Notably, the precise
200 relative timing between surround (t_s) and center stimulation onsets (i.e., -70, -40, or -25 ms) or
201 surround stimulation duration (5, 20, or 50 ms) had little impact on the amplitude variance of
202 surround-triggered inhibitory postsynaptic currents (*see* arrow, Fig. 1d) or on the relative impact of
203 center modulation. This mainly stems from latency differences in signaling between center and
204 surround, with surround *E* and *I* conductances peaking at average latencies of 20 and 28 ms,
205 whereas center conductances peaked at 9 and 15 ms, respectively (Supplementary Fig. 3d).
206
207 Surround network activation typically generated a variable combination of excitation and inhibition in
208 terms of amplitude and timing. However, during the onset of center stimulation (t_c), only the inhibitory
209 components persisted while any remaining excitation was quenched due to the relatively faster
210 transmission of synaptic excitation (*see* Supplementary Fig. 2). This can be seen by the non-null
211 values of surround-triggered outward currents when holding at 0 mV at t_c (*see* arrow, Fig. 1d and 1i).
212 As expected, removal of surround input via pharmacological blockade of $GABA_A$ receptors using
213 bath-applied gabazine (GBZ) transformed any input into seizure-like activity while saturating
214 subsequent center response profiles (bottom traces in Fig. S2a).
215
216 To test how surround signaling can account for the observed modulation of center excitability, we
217 calculated the theoretical contributions of excitatory (G_e) and inhibitory (G_i) synaptic conductances
218 [33,34] during center only (magenta) and center-surround interaction (cyan) in Figure 1f. Here, the
219 relationship between inhibition and excitation of the recorded neuron plotted in Figure 1d is shown
220 during these two conditions (*see* also Fig. S3). Notably, consecutive center stimuli (C_1-C_2) reveal
221 that inhibition can increase to nearly double the levels while simultaneously maintaining twice the
222 levels of excitation compared to the significantly decreased levels evoked by surround-center
223 stimulation (S-C_s). This result suggests that center-surround interactions reduce the persistence of
224 both types of inputs. This was true for the majority of SCs interneuron cell types, with over half of
225 them being classifiable based on either morphology (i.e., horizontal, wide-field, narrow-field, or
226 stellate; for details, *see* [35]) or genotype (e.g., vGAT+; *see* Fig. S4 for quantification). We found that
227 peak excitation (G_e: mean amplitudes of C_1: 1.7 ± 0.3 nS and C_s: 0.6 ± 0.1 nS with a mean percentage
228 decrease of 62.3 ± 4.7%) and peak total conductance (G_t: mean amplitudes of C_1: 2.1 ± 0.3 nS and
229 C_s: 1.2 ± 0.2 nS with an average percentage decrease of 40.6 ± 5.3%) of the center response was
230 significantly reduced following surround network activation in all these recordings (Fig. 1g and Fig.
231 S3), while no significant accompanying increase was observed on average to the center inhibition
232 at peak G_t (Fig. 1h; mean amplitudes of C_1: 0.53 ± 0.08 nS and C_s: 0.55 ± 0.09 nS).

There are two explanations for this weakening of the center excitatory conductance: (i) inhibitory conductances persisting at t_c, which might act linearly or non-linearly, and/or (ii) a lesser number of active inputs arising from local glutamatergic interneurons contributing to the center response. Although a weak, yet statistically significant, correlation was observed between the inhibitory conductance at t_c (mean amplitude ± s.e.m.: 0.46 ± 0.08 nS, p = 0.004, n = 24) and the reduction in the center peak G_e (Fig. 1i), the low slope value indicates that it can only account for a partial explanation of the observed decrease in center excitation. Hence, both center and surround zones reciprocally affect each other through synergistic recurrent interactions among local populations of excitatory and inhibitory neurons, aiming to reduce the overall levels of excitation in the system (Fig. 1j).

SCs space defined by local recurrent excitatory and inhibitory circuit motifs

At the network level, this reduction of center activity can be achieved by: 1) direct activation of long-range inhibitory neurons in the surround, 2) indirect activation of inhibitory neurons in the center via excitatory neurons in the surround, or 3) a combination of both mechanisms. To reveal the underlying circuit motifs, we performed retrograde trans-synaptic labeling from either vGluT2 or vGAT neurons to identify their monosynaptic and presynaptic sources of excitatory and inhibitory input in the SCs. Considering their comparable proportions (i.e., 40% vGluT2 and 60% vGAT; *see* [36]) and their intermingling within the SCs, we opted for genetically restricted approaches to accurately target and classify these neurons based on their neurotransmitter.

To trace local afferent input to excitatory and inhibitory neurons restricted within the boundaries of the SCs layer, an AAV-DIO-TVA-V5-RG was microinjected (50 nL) into the SCs of adult (older than 58 days) vGluT2- and vGAT-Cre mice (Fig. 2a and Fig.S5). This Cre-dependent AAV helper vector was designed to express the TVA receptor together with the engineered rabies glycoprotein (RG; *see* [37,38] exclusively in either excitatory or inhibitory neurons depending on the mouse line used. The injection of the helper virus was delivered into the SCs layer to ensure that neurons expressing the RG would be located within the SCs layer, thereby minimizing spillover into the intermediate layers (SCi) as indicated by the green box in the coronal midbrain section of Figure 2b. Any cases where helper expression extended beyond the boundaries of the SCs were excluded from the analysis. Three weeks later, the enhanced green fluorescent protein (EGFP)-expressing EnvA-coated and G-deleted rabies (Rb; *see* [39] viral vector was injected, targeting the same location in the SCs as the helper virus injection (Fig. 2a-b).

Neurons that were transfected with the Cre-dependent helper virus, as detected by V5 immunohistochemistry, which would also express Rb-EGFP were referred to as 'starter' neurons (Top, Fig. 2c). Therefore, in experiments involving vGluT2-Cre animals (N = 3), vGluT2+ excitatory

cells served as starter neurons, while in experiments with vGAT-Cre animals (*N* = 3), vGAT+ inhibitory cells were the starter neurons. On the other hand, cells labeled solely with Rb-EGFP, without the presence of the V5 tag, were classified as input neurons, providing monosynaptic input to the starter neurons (Fig. 2c). Rather than performing a whole-brain input analysis in the SCs (*see* [40], we focused on shedding light on the local connectivity between vGluT2+ and vGAT+ neurons in the SCs. We quantified the total number of presynaptic input neurons (Fig. 2c; *see* also Fig. 2g) and examined the spatial distribution (Fig. 2e-f) onto each other within the SCs, as well as long-range inputs arising from both retinas.

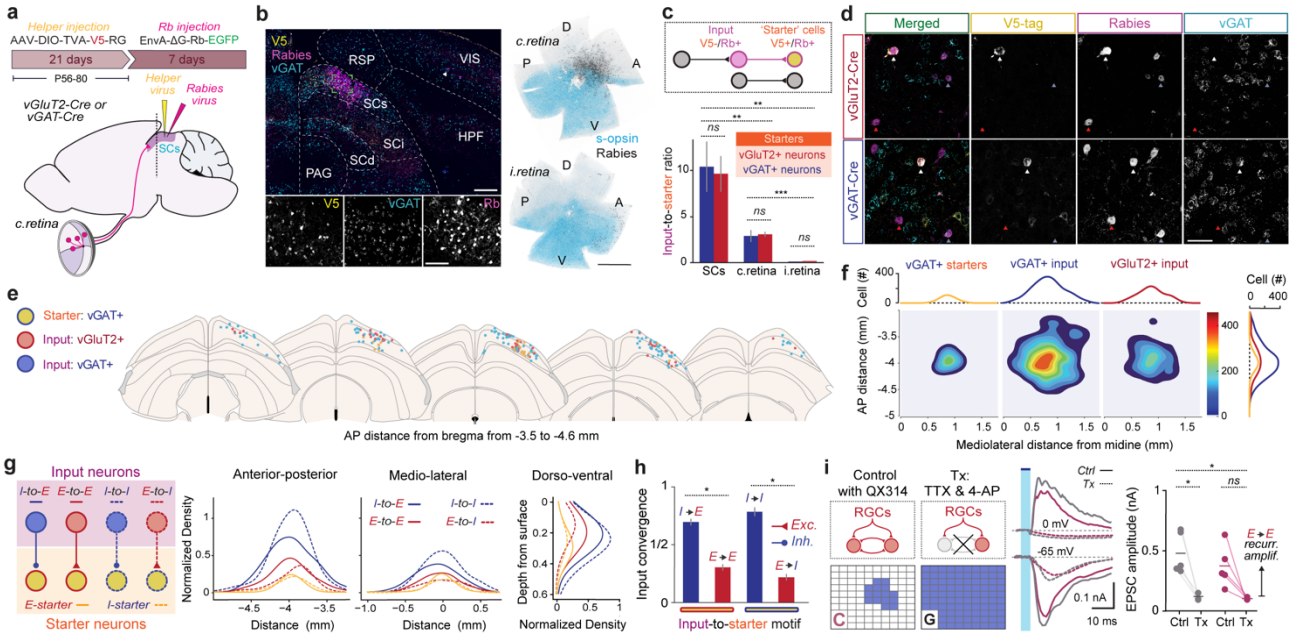

Fig. 2: Connectivity between local excitatory and inhibitory motifs in SCs space

(a) The helper virus AAV-DIO-TVA-V5-RG expresses the rabies glycoprotein (RG), and a fusion of the TVA receptor with the V5 tag. The RG-deleted rabies virus Rb, pseudotyped with EnvA, expresses EGFP. The AAV helper virus was first injected into vGluT2-Cre (*N=3*) and vGAT-Cre (*N=3*) mice and 3 weeks later the Rb-EGFP was delivered in the same location in the SCs.

(b) Left: coronal section of the midbrain of a vGAT-Cre animal with emphasis on initial injection site where expression of the V5 tag (in yellow) should be restricted to and not beyond the SCs layer. Subsequently, EGFP-expressing neurons are a result of Rb-transfection (magenta). Scale bar: 300 µm. Insets below show colocalization of the enlarged area (green box). Scale bar: 100 µm. Right: Contralateral and ipsilateral retinas showing retinotopy of presynaptic Rb-EGFP RGCs (black). Counterstaining with s-opsin (light blue) reveals retinal orientation. Dorsal, D; anterior, A; ventral, V; posterior, P. Scale bars: 1000 µm.

(c) Top: starter neurons are identified based on the co-expression of the V5 tag and Rb-EGFP. Input neurons only express Rb-EGFP and provide monosynaptic and presynaptic input to the starter neurons. Bottom: Input convergence shows the ratio of input-to-starter neurons arising from: i) within the SCs, ii) contralateral (*c.*), and iii) ipsilateral (*i.*) retina.

(d) RNAscope ISH for vGAT (for vGluT2, *see* Fig. S5) revealed the identity of Rb-EGFP input neurons while confirming starter neuron cell-types. White arrows indicate starter neurons, whereas red and blue show excitatory (*E*) and inhibitory (*I*) input neurons, respectively. Scale bars: 50 µm.

(e) Schematic depicting the dorsoventral and mediolateral location of starter and input neurons in five separate anterior-posterior (AP) coronal sections of the SCs layer in a vGAT-Cre animal.

(f) Contour plot showing the spatial distribution of *E* and *I* input neurons to *I* starter neurons in the AP and medio-lateral ML dimensions across the SCs (for case shown in **e**).

(g) (Left to right) Schematic of all possible motifs between input and starter neurons. The next three panels show the quantitative relationship between the density of input neurons and starter neurons for *E* and *I* cell types across the three anatomical dimensions (AP, ML and DV). Solid lines depict data obtained

from excitatory starters averaged from vGluT2-Cre animals (*N*=3), whereas dashed lines show data obtained from inhibitory starters averaged from vGAT-Cre animals (*N*=3). *See* Fig. S5e for the distributions obtained from individual animals.
(h) Quantitative cell-type-specific input-to-starter ratios (referred to as *input convergence*) reveal feedforward (i.e., *E-I* and *I-E*) and recurrent connectivity patterns (i.e., *E-E* and *I-I*). Comparison of means performed using a *t*-test.
(i) Excitatory and inhibitory current recordings (at -65 and 0 mV) from SCs neurons (*n=5*) were performed in response to center (C) and global (G) optostimulation conditions of ChR2-expressing RGC axonal terminals. Bath application of 1 μM TTX and 100 μM 4-AP isolate monosynaptic RGC-triggered excitation while simultaneously abolishing recurrent excitation and recruited feedforward inhibition. Mean evoked EPSC amplitudes ± s.e.m.: from left to right, for Ctrl: 0.40 ± 0.08 nA; for Tx: 0.02 ± 0.01 nA; for Ctrl: 0.29 ± 0.08 nA; for Tx: 0.010 ± 0.004 nA. RM one-way ANOVA, p = 0.0072; Tukey's multiple comparisons test, p(global-Ctrl *v.s.* global-Tx) = 0.0382, p(global-Ctrl *v.s.* center-Tx) = 0.0308, p(center-Ctrl *v.s.* center-Tx) = 0.0821. Washout not shown for clarity.
Abbreviations: HPF, hippocampal formation; *Ctrl*, control condition; and *Tx,* treated condition.

We found that vGluT2+ and vGAT+ starter neurons received a similar number of inputs from ipsilateral SCs interneurons (mean ± s.e.m.: 9.5 ± 2 and 10.2 ± 2.8 cells, respectively) but also long-range inputs from both contralateral (2.9 ± 0.3 and 2.8 ± 0.7 cells, respectively) and ipsilateral RGCs (0.07 ± 0.01 and 0.03 ± 0.02 cells, respectively). As expected, the retinotopic pattern is observed (right of Fig. 2b), with contralateral RGC input mainly originating in central regions and ipsilateral RGC input restricted to peripheral regions of the retina, reflecting our systematic viral targeting of the middle region along the mediolateral (ML) and anteroposterior (AP) axes of the SCs (Fig. 2a and 4a). To determine whether the Rb-EGFP+ input cell types were excitatory or inhibitory, we performed RNAscope *in situ* hybridization (ISH) targeting the vesicular GABA transporter (vGAT) or the vesicular glutamate transporter 2 (vGluT2; Fig. 2b and 2d). Neurons that were negative for vGAT, were positive for vGluT2 and vice versa. Figure S5 shows that co-staining Rb-EGFP+ cells with vGluT2 and vGAT probes did not display colocalization, while nearly all detected input cells (269 out of 272 in *N* = 2 animals) were labeled by only one of these two probes.

The relative spatial distributions of vGluT2+ and vGAT+ starter and input neurons were determined by counting the neurons expressing V5 and/or RV-EGFP and mapping their location onto the Allen Reference Atlas coordinate system across the SC layer (Fig. 2e-f and Supplementary Fig. S5e; *see* Methods for details). In Figure 2e, a representative example of a vGAT-Cre animal is shown, illustrating a small number of concentrated inhibitory starter neurons (V5+ and Rb-EGFP+; depicted as yellow dots) together with a broader distribution of input neurons (Rb-EGFP+), which were further classified based on their neurotransmitter type as excitatory (red dots) or inhibitory (blue dots). For all animals, we determined the mediolateral (ML), anteroposterior (AP), and dorsoventral (DV) distribution using this approach for each starter and input neuron, as well as their respective cell type classification (Supplementary Fig. 5e).

The Gaussian kernel-based density plots in Figure 2f reveal the horizontal distribution patterns along the ML and AP dimensions (*see* Methods) of the representative example shown in Figure 2e. Inhibitory starter neurons (left panel in Fig. 2f) were observed to occupy a confined retinotopic area

350 within the SCs, influenced monosynaptically by a broader excitatory area (right panel in Fig. 2f), as
351 well as an even broader inhibitory area (middle panel), thereby, receiving visual input from RGCs
352 located across larger retinal regions. At peak density, the inhibitory starters were found to receive
353 synaptic input from more than double as many inhibitory input neurons establishing a motif of
354 recurrent inhibition (Fig. 2f-g).
355
356 Using this approach applied in all animals (*N* = 6), we found that every possible motifs between input
357 and starter neurons existed (Fig. 2g-h and Supplementary Fig. 5e). In Figure 2g, color-coded solid
358 lines represent average spatial distributions using excitatory neurons as starters, while color-coded
359 dashed lines correspond to those from inhibitory starters (*see* Fig. S5e for individual traces). As
360 expected, input neurons always display higher normalized density distribution compared to their
361 starter counterparts. Notably, while *I-E* and *I-I* input-to-starter connections span a broader range on
362 the ML, AP and DV axes, a stable E/I ratio is maintained throughout the SCs, with no identifiable
363 asymmetries arising from a specific connection. By contrast to excitatory neurons, inhibitory inputs
364 exhibited stronger connections with both inhibitory starter neurons (78.8 ± 4.6%, n = 3) and excitatory
365 starter neurons (69.2 ± 2.3%, n = 3). The remaining proportion was accounted for by excitatory input
366 neurons. Notably, about one third of excitatory input neurons establish monosynaptic contact with
367 excitatory starter neurons (second column in Fig. 2g), thereby, establishing a local recurrent
368 excitatory network that can be also triggered by monosynaptic long-range RGC input (Fig. 2b).
369
370 Figure 2i demonstrates the efficacy of the recurrent excitatory connection (*E-E)* by recording SC
371 neurons (*n* = *5*) in response to optostimulation of RGC terminals within their identified center zones
372 in the presence of 1 μM TTX and 100 μM 4-AP (washout *not shown* for clarity). Evoked EPSC
373 amplitudes were drastically reduced by about ~90%, with a small component persisting resulting
374 from monosynaptic RGC input (Fig. 2i, mean amplitudes ± s.e.m.: for Ctrl: 405.5 ± 81.1 pA; for Tx:
375 22.3 ± 11.0 pA). This observation suggests the existence of additional center-dependent excitatory
376 input (Fig. 2d, 2g-h and S5e), which may serve to amplify incoming visual signals. Furthermore, the
377 lack of observed outward currents (traces held at 0 mV) during this treated condition (Tx) indicates
378 the removal of recruited di- or oligo-synaptic inhibition, thereby exposing the indirect functional
379 impact of local *I-E* and *I-I* inputs (Fig. 2i). As expected, the similar response profiles observed
380 between center-specific and whole-field (global) optostimulation indicate that most of the *E-E* input
381 is generated within the neuron's center zone.
382
383 **Local recurrent excitation and feedback inhibition drives visual surround suppression**
384 To isolate the contribution of different connections (*E-E, E-I, I-I,* and *I-E*) to the center-surround
385 interactions in Figure 1d-j, we constructed a large-scale model consisting of 12,800 spiking neurons
386 to simulate the SCs layer. The model was constrained by the measured input convergence ratios
387 and spatial distributions (Fig. 2g-h, Supplementary Fig. 5e) summarized in the cartoon in Figure 3a.

To quantify these network interactions, we used a spiking neuron model with conductance-based synapses, which were connected to each other based on physical distance according to a Gaussian connectivity kernel (*see* Table 3 and Supplementary Fig. S4e). Because we were interested in the contribution of different connections, we kept the connection probability and distance-dependent connectivity kernel fixed and systematically varied the connection strengths (*see* Table 3-7). For all synaptic strengths the network remained in an inhibition-dominated activity regime in which inhibitory neurons displayed a higher background activity than excitatory neurons [41].

To mimic center zone activation, we triggered activity in 314 excitatory and 314 inhibitory model neurons in four conditions (Fig. 3b-d) and measured the evoked excitatory synaptic conductance in a randomly chosen neuron from the center region (Fig. 3e). First, the center neurons alone were stimulated (*see* no.1 in Fig. 3b, top row in Fig. 3c and first column in Fig. 3d). As with our experimental recordings (*see* Fig. 1d), model center response patterns typically demonstrated multiple peaks, often characterized by a dual peak profile (green trace in Fig. 3e). The first peak is provided monosynaptically by glutamatergic RGC input and followed by a second peak that indicates that center stimulation engaged activity in neighboring unstimulated excitatory neurons. As expected, the second peak depended mainly on the strength of recurrent excitatory connection (*E-E*) and was also found to covary with the strength of the *I-E* connection (Fig. 4f).

When center stimulation was immediately followed by a surround input (*see* #4 in Fig. 3b, bottom row in Fig. 3c and fourth column in Fig. 3d), the peak of the secondary response was determined by the mutual coupling between excitatory and inhibitory neurons (blue traces in Fig. 3e). In line with our results presented in Fig. 1, the initial surround-induced inhibitory conductance persisted after the removal of surround inputs, effectively attenuating the secondary response to below threshold (yellow line in Fig. 3e). This occurred because fewer *E* and *I* neurons could respond beyond threshold to the center input (bottom row in Fig. 3c). This was further supported by the observation that secondary response attenuation was more pronounced when center input coincided with the presence of surround input (red traces in Fig. 3e). Even though center and global responses are comparable in amplitude (Fig. 2i), confirmation of this prediction was not possible experimentally as center responses would prevail during the simultaneous optogenetic activation of center and surround (*see* #3 in Fig. 3b and third column in Fig. 3d).

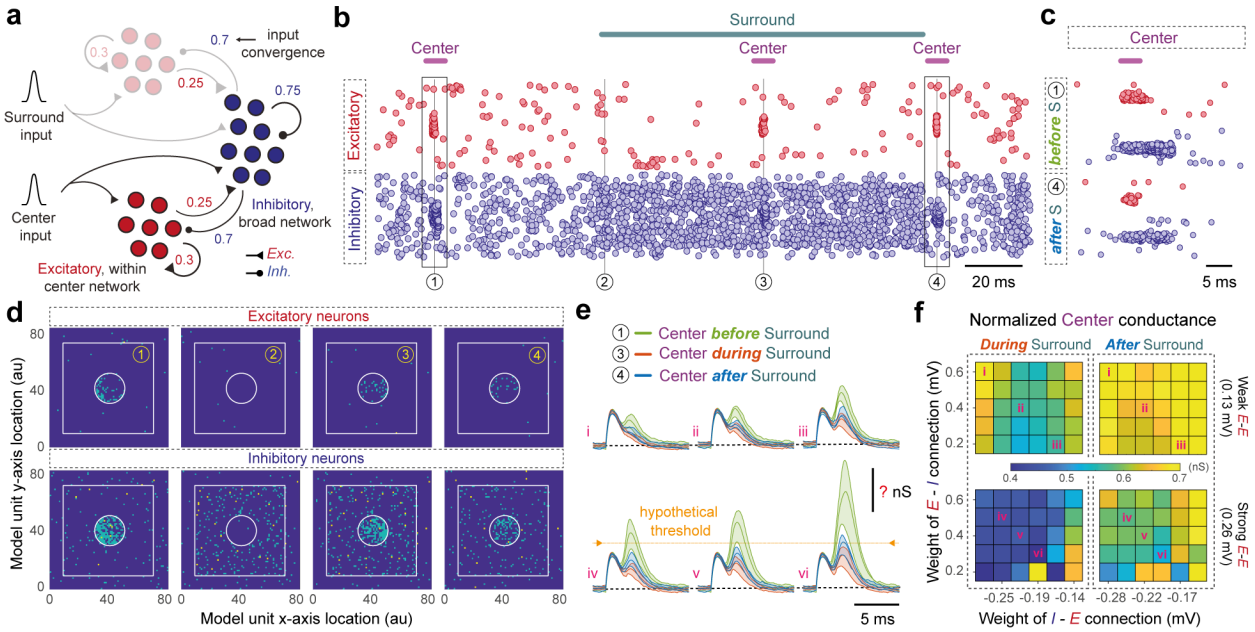

Fig. 3: Model predicts recurrent networks a key feature in visual surround modulation

(a) Schematic of the network model using E/I connectivity patterns shown in Fig. 2g. 6400 excitatory and 6400 inhibitory neurons were placed on a square lattice which was folded as a torus to avoid boundary effects (*see* **c**).

(b) Raster of spiking activity with four stimulus conditions that are marked with vertical numbered lines that simulate experimental conditions shown in Fig. 1. Conditions *1:* center only before surround, *2*: surround only, *3*: center during surround, and *4*: center after surround)

(c) Expanded network response of conditions 1 (top) and 4 (bottom) shown in (b).

(d) Spatial arrangement of center and surround network response profiles during the 4 different stimulus impulse conditions. The square schematically shows the region in which neurons were placed on a square grid. Excitatory (top) and inhibitory neurons (bottom) within the white circle received inputs corresponding to the center stimulation. All the neurons in white square but outside the inner circle received inputs corresponding to the surround network. Each subplot shows activity measured within a bin of 5 ms.

(e) Time courses of excitatory conductance of a center neuron. Each trace is an average of 20 trials and shading indicated 25%-75% quartiles. The first peak is generated with low-variance monosynaptic activation of direct retinal input whereas the second peak is a network effect generated by balanced recurrent excitation and recurrent inhibition. The connectivity parameters for these six examples are marked in panel **(f)** with Latin numerals.

(f) Normalized center conductance during and after surround stimulation. Each colormap shows normalized change in excitatory conductance (*see* Methods) in a center neuron (shown in panel e) as a function of recurrent excitation (top: weak connection; bottom: strong connection) and mutual connectivity weights between excitation and inhibition (x-axis: inhibition of excitatory neurons; y-axis: excitation of inhibitory neurons).

To quantify the contribution of individual circuit motifs, we normalized the center response during and after surround input (left and right column in Fig. 3f) by the peak when only center input was delivered (Fig. 3f). As expected, any increase in the *I-E* connection increased its attenuation, whereas *E-I* connectivity did not have a strong effect on the attenuation of the secondary peak. Notably, increase in the strength of recurrent excitation also increased the attenuation of the secondary excitatory conductance peak (compare top and bottom rows in Fig. 3f). The effect of surround-triggered inhibition on center excitation was larger when center input arrived in the presence of an active surround (left column in Fig. 3e). Overall these results demonstrate the

457 reduction in excitatory conductance during surround suppression requires both recurrent *E-E* and *I-*
458 *E* connections.
459
460 **Center activation lowers E/I balance of active SCs neurons in the surround**
461 Results obtained from the circuit mapping (Fig. 2c and 2g-h) corroborated with the simulated network
462 (Fig. 3e–f) indicate that the balance between excitation and inhibition (E/I) should shift to lower
463 values in the surround region when the center is stimulated. To test this prediction, we intravitreally
464 injected wild-type C57BL/6NCrl mice with an AVV2-ChR2-EYFP (*N* = 5) or AAV2-mCherry (*N* = 3,
465 for control) to express ChR2 (or a control protein) in RGC axonal terminals (top, Fig. 4a). The
466 successful activation of SCs neurons following *in vivo* optostimulation of RGC terminals via an
467 implanted fiber optic unilaterally was confirmed through *cFos* labeling, a surrogate marker of neural
468 activity (Fig. 4a-b). The animals were maintained in a dark chamber to eliminate the potential
469 influence of natural visually driven activity.
470
471 Figure 4b shows the distribution of active SCs cells in coronal sections (top is control, bottom is
472 ChR2). After control optostimulation, the presence of a sparse population of spontaneously active
473 neurons located could be seen reflecting baseline activity at approximate equidistant locations along
474 the mediolateral axis with a higher concentration near the midline (top image in Fig. 4b).
475 Optostimulation of ChR2-expressing RGC axonal terminals (bottom image in Fig. 4b; *see* Methods)
476 revealed a significant increase in *cFos* expression under the implant (top, Fig. 4c), with higher overall
477 levels observed across both hemispheres (bottom, Fig. 4c). Furthermore, during control the spatial
478 distribution of active neurons across the mediolateral axis maintained a balance across the
479 hemispheres, which shifted in the case of ChR2-expressing RGC input activation (bottom, Fig. 4b).
480
481 Shifts in E/I balance were determined by quantifying the proportion of inhibitory neurons among the
482 total activated cells. To do this, we defined the center region as the area located directly under the
483 implant (C), along with two distal surround zones located more than 400 μm from the center: a medial
484 surround zone (SM) and a lateral surround zone (SL). Figure 4d (top) shows a subset of *cFos* positive
485 neurons in the center zone that were immunoreactive for the neurotransmitter GABA revealing their
486 inhibitory origin (*see* also Supplementary Fig. S7). Notably, optostimulation drives a balance of
487 excitation and inhibition in the center with a population of putative glutamatergic neurons (i.e.,
488 negative for GABA) that matches the population size of active inhibitory neurons (C: 0.49 ± 0.07, *N*
489 = 4; mean ± s.e.m.). The fraction of colocalized neurons, however, shows a significant increase in
490 the ratio of active GABAergic neurons in both surround zones compared to the center (SM: 0.70 ±
491 0.13, SL: 0.73 ± 0.14, *N* = 4; mean ± s.e.m.). This finding supports the notion that there will be fewer
492 recurrent excitatory neurons active to amplify visual signals in the surround when the center is active,
493 and vice versa.
494

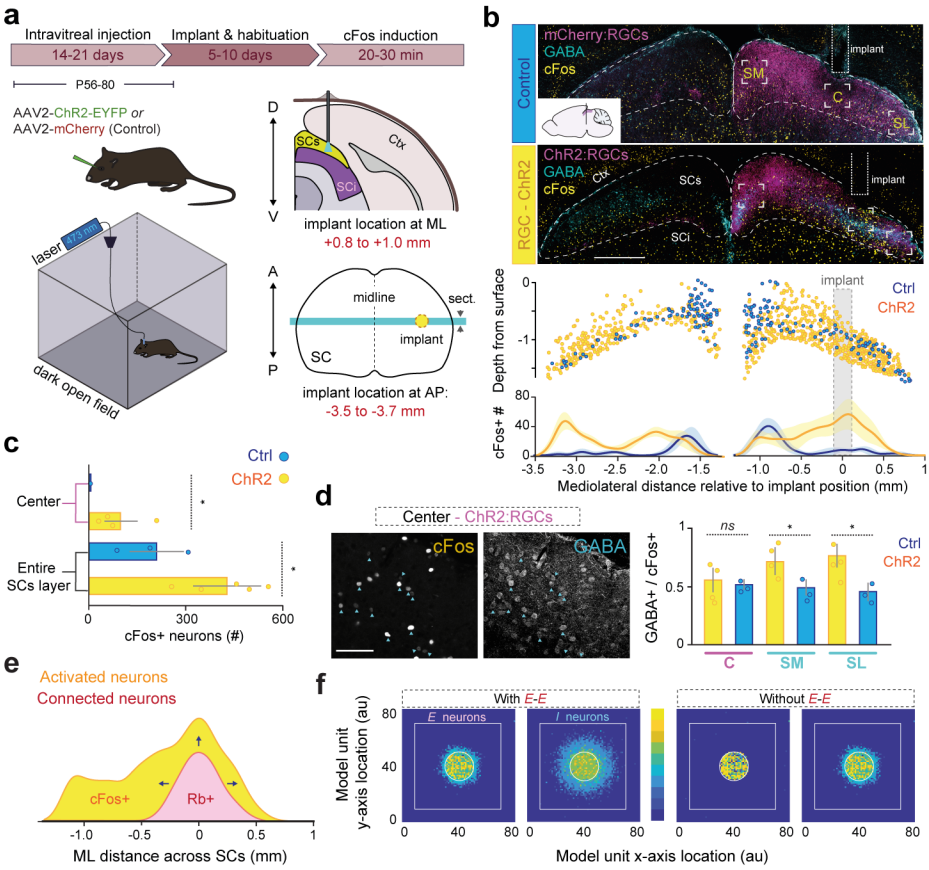

Fig. 4: Functional identification of active SCs neurons reveals that center activation lowers E/I balance in the surround

(a) Pipeline that we used to measure *in vivo* cFos expression induced by local optostimulation of RGC axonal terminals in the SCs. Top left: As in Fig. 1a, expression of ChR2 in RGCs was achieved using an intravitreal viral injection of the vector rAAV2-hsyn-hChR2(H134R)-EYFP (in WT mice, *N=5*) or rAAV2-hsyn-mCherry for control (in WT mice, *N=3*). Bottom left: schematic illustrating assay performed in a dark box. Right panels: cartoon of the optic fiber placement site shown in a coronal (top) and a horizontal (bottom) midbrain sections.

(b) Top panels: Coronal midbrain sections of the SCs centered around the implant for c-*Fos* induction following local optostimulation. Yellow, c-*Fos* immunostaining; magenta, control (top) or ChR2 (bottom); cyan, GABA immunostaining. Scale bar represents 500 µm. *Abbrev*: C, center; SM (surround medial); SL (surround lateral). Bottom panels: The location (top) and distribution (bottom) of c-*Fos* positive neurons across the hemispheres of the SCs. Blue circles are control; Yellow circles are ChR2-induced. The central zone (C) is defined by the implant tip, which defines the origin of the x-axis. Shading is standard error.

(c) Comparison of the total cell count of cFos+ cells induced in SCs neurons between control (in blue, *N=3*) and during activation of ChR2-expressing RGC axonal terminals (in yellow, *N=5*) across the entire SCs layer and center zone, respectively.

(d) Top: Grayscale image taken from the center region showing c*Fos* (left) and GABA immunostaining (right). Blue arrows show colocalization. Bottom: Ratio of GABA+ to c*Fos*+ cells across the three zones (C, SM and SL) compared between the two conditions (ChR2-induced, *N=4*; and control, *N=3*). Statistical testing was done using Student's *t*-test (*, $p < 0.05$; ***, $p < 0.0001$; *ns*, no significance). Bars show standard error of the mean.

(e) Comparison of the distribution between activated and connected neurons. Plot of activated neurons (in yellow) was obtained from the bottom right panel in **(b)**, whereas the plot of connected neurons (in red) was obtained using cell-type-specific transsynaptic retrograde mapping shown in Fig. 2 and Fig. S5.

(f) Qualitative comparison of the effect with (top) and without (bottom) the recurrent *E-E* connection on the distribution of active neurons in response to center stimulation using the same model parameters used in Fig. 3. The square schematically shows the region in which neurons were placed on a square grid (as in Fig. 3d). Inner circle is the site of center stimulation, whereas the surround is located between the inner white square excluding the area occupied by the white circle. Probability of spiking (estimated

from 20 trials) of a neuron when center alone was stimulated. The color bar ranges from 0 to 1 and shows the probability of spiking when the center is stimulated.
Abbreviations: C, center; SM, surround medial; SL, surround lateral.

Figure 4e compares the spatial distribution between activated neurons (data from Fig. 4b) and connected neurons (data from Fig. 2g and Supplementary Fig. S5e). Considering the unlikely event of activated fibers of passages targeting areas other than the center [42], which may contribute to this discrepancy, two plausible reasons can be identified: 1) activation of retinotopically-aligned recurrent networks and 2) activation of upstream circuits connected to the SCs arising, for example, from the V1 and parabigeminal nucleus (Fig. 4e). To explore whether local recurrent excitation can account for the observed drop in the surround E/I balance mediated, we tested the efficacy of the connectivity footprint by increasing the intensity of the model's center stimulation while utilizing the same parameters as depicted in Fig. 3 (refer to Table 5 for details). When recurrent excitatory connections were active (top row in Fig. 4f), center stimulation triggered neuronal activity in the surround that was not directly stimulated as indicated by the non-zero firing probability in neurons outside the white circle depicting the model 'center' (Fig. 4f). Recruited responses in inhibitory neurons spread out more than in excitatory neurons indicating the spatial discrepancy between the *E-E* and *E-I* connections, which we found to be independent of center size. This qualitative description obtained by the model simulation could explain shifts in surround E/I without the exclusive reliance on long-range horizontal connections.

Discussion

This study offers mechanistic insight into how the SCs computes visual saliency through recurrent-based center-surround interactions, capable of operating independently yet in parallel with other extraretinal brain regions like V1. Targeted optogenetic activation of center and surround zones in individual neurons allowed us to test the presence and circuit implementation of surround modulation, using the SCs as a conserved model of early visual processing. Our experiments show that a selective decrease in center excitation occurs when the visual surround is active (Fig. 1); a potential computation contributing to midbrain target selection where a current central input becomes the next saccade's surround input. Given our experimental settings, this result proves that evoked changes in synaptic excitatory conductance of varying magnitude (usually moderate or strong) are due to local interactions placed within the midbrain SCs itself. This finding suggests that the main extraretinal circuits (i.e., SCs and V1) belonging to divergent subcortical and cortical pathways can perform surround suppression independently. This implies that a stimulus can undergo selective suppression in one pathway (e.g. thalamocortical) while concurrently being preferred in the other (e.g. retinotectal). Understanding how phylogenetically older and neocortical circuits can cooperate or compete is important for comprehending the versatility in pre-attentive visual processing.

As in cortical circuits [43], the SCs also contains excitatory and inhibitory neurons that are spatially intermingled, a feature that complicates the unravelling of their function. By combining intracellular measurements (Fig. 1) and connectivity analysis (Fig. 2) with a computational model (Fig. 3), we revealed two main local circuit motifs: recurrent excitation (*E-E*) and feedback inhibition (*I-E*) that contribute to surround suppression in distinct ways. *E-E* connections amplify responses in a specific retinotopic 'center' whereas *I-E* performs a dual function. It overlaps with center-specific *E-E*, thereby modulating the responses of the same center neurons subject to *E-E*, while simultaneously, reaching slightly beyond this zone, curbing the responsiveness of neighboring surround neurons outside the center (Fig. 2–3). In natural conditions, however, every input should be accompanied by some surround input since one neuron's center will be another neuron's surround. We show that in such a case, these recurrent interactions conspire to reduce the persistence of input in the absence of top-down input. Further research is required to establish whether multiple classes of inhibitory interneurons are involved in specific computations in the SCs, drawing parallels to findings in V1 where the potential role of somatostatin-positive [44] in coalition with recurrent excitatory connections [45] are involved in cortical surround suppression.

The question of whether these networks process all visual streams uniformly, with each stream conveyed by distinct RGC subtypes (of which more than 30 are known, *see* [49], can be addressed in future by using our approach presented in this study. For instance, can some inputs bypass this circuitry, evade surround suppression, and avoid engaging *I-E* subcircuits? Can they selectively drive surround facilitatory connections for contour integration across the visual layer [50]? This can be addressed by optostimulating specific RGC subtypes using opsins expressed in specialized Cre-lines (e.g., Kcng4-Cre for targeting alpha RGCs, *see* [51]), instead of a panretinal approach. This strategy can be taken beyond sensory systems, interrogating the presence and nature of center-surround interactions in modular architectures within motor systems that would be technically challenging to address *in vivo*. The functional receptive field mapping approach designed in this study can provide key insight into local circuit function and underscores the need for developing approaches that link such local processes to global network function.

Visual saliency computations in the SCs provide cortical circuits the flexibility to modulate SCs activity either by amplifying or suppressing with retinotopic correspondence (*see* white arrow in Fig. 2b, *see also* [27]). This could allow them to engage with SCs recurrent networks and modulate local center-surround dynamics in a top-down manner. For instance, by granting selective access for pyramidal neurons in V1 to interact with *E-E* connections, responses can be biased to specific incoming retinal inputs from certain areas of the visual field, or in contrast, they can be suppressed by activating *I-E* connections. Importantly, these phylogenetically conserved circuits in the SCs can also influence cortical activity via tecto-thalamic pathways [52], thereby influencing visual attention [30,53]. This highlights the ability of SCs activity to modulate neural activity in both upstream and downstream

605 targets, potentially influencing higher-order functions like visuospatial perception and behavioral
606 selection.
607
608 Taken together, our results show that selective decrease in center excitation when the visual
609 surround is active is consistent with models that involve amplification in recurrent networks [46], but
610 inconsistent with models that are dominated by feedback inhibition [47]. In the latter, transient increase
611 in inhibition would account for reduction in overall excitation and inhibition levels – an outcome that
612 our measurements did not support. Computational models of trial-by-trial variability suggest that,
613 while both increases in inhibition or decreases in recurrent excitation can similarly affect the average
614 output response, the latter is more likely to minimize variability across trials [48]. We propose that SCs
615 circuitry has evolved to mitigate this variability where surround inputs are continuously transformed
616 into center inputs during visual exploration.
617

618 ## Acknowledgements

619 We thank Drs. Michael Haüsser, Abdel El Manira and Julien Bouvier for comments on the
620 manuscript. We thank Dr. Sten Grillner for his support throughout this study. We thank Drs. Mats
621 Hellström and Sias Jordaan for technical assistance. A.A.K. acknowledges funding from the Swedish
622 Research Council (Starting Grant in Medicine no. 2016-03134 and Project Grant in Medicine no.
623 2020-02927), CIDEGENT funding from the Valencian Community in Spain (no. 2021-028), Strategic
624 research area neuroscience StratNeuro (Start-up program 2017), the Swedish Brain Foundation
625 (Hjärnfonden no. FO2018-0254), the Hedlunds Foundation (no. M-2017-0691) the Olle Engvist
626 Foundation (no. 196-0148) and the Stiftelsen Kronprinsessan Margeratas Arbetnämnd för
627 synskadade (nos. 2019-027 and 2020-182).
628

629 ## Author Contributions
630

631 P.C. performed electrophysiological recordings, viral injections, optogenetic experiments and data
632 analysis. K.S. performed neuroanatomical experiments, RNAscope *in situ* hybridization, viral
633 injections, fiber implantations and data analysis. D.M.M. performed *in vivo* cFos induction
634 experiments, visualization of neuroanatomy, and data analysis. A.G.I. performed
635 electrophysiological recordings. I.L. and T.F. contributed to neuroanatomy and *in vivo* experiments.
636 A.A.K. performed the conductance analysis. I.L., K.M., T.F., and A.A.K contributed to the
637 conceptualization and experimental study design. K.M. contributed vectors and resources for
638 visualization of neuroanatomical data. A.K. contributed to the computational study design and
639 performed the numerical experiments. A.A.K. designed the figures, supervised and funded the study.
640 A.A.K. wrote the manuscript with help from A.K. All authors reviewed and commented on the
641 manuscript.
642

643 ## Lead contact

644 Further information and requests for sources should be directed to and will be fulfilled by the lead
645 contact, Andreas Kardamakis (akardamakis@umh.es).
646

647 ## Material and Methods

648 **Animal strains**

649 Experimental procedures were approved by the Stockholm municipal committee for animal
650 experiments and the Karolinska Institute in Sweden (N9179-2017 and N6747-2019 to A.A.K.), as
651 well as, the Committee on Animal Research at the Universidad Miguel Hernández and carried out in
652 compliance with the Research Council of Spain (CSIC), the Generalitat Valenciana (GVA) and
653 European regulations (2022/VSC/PEA/0236 to A.A.K.). Both male and female vGAT-Cre (Jackson:
654 Slc32a1tm2(cre)Lowl), vGluT2-Cre (Jackson: Slc17a6tm2(cre)Lowl) and wild-type mice (C57BL/6N;
655 Charles River) were used throughout the experiments. Mice were kept on a 12-h day/night cycle
656 under stable temperature (21 ± 1 °C) and air humidity (50–65%) with freely available food and water.
657 The exact numbers of cells (*n*) and animals (*N*) used for each experiment are reported in the *Results*
658 section and corresponding figure legend.
659

660 **Viral injections**

661 The complete list of viruses we used is provided in Supplementary Table 1. Injections were
662 performed in 2–5 months old wild-type mice and transgenic mice under isoflurane anesthesia and
663 injected with buprenorphine post-surgery. Viral titers of adeno-associated viruses (AAV) and
664 modified rabies virus were between 1×10^{12} and 1×10^{13} viral genomes per milliliter (vg/mL). To
665 express ChR2 in the axons of RGCs in the superficial layer of the right hemisphere SC, we injected
666 1000 nL into the vitreous bodies of the left retinas using the following viral vectors:

667 1.rAAV2/hsyn-hChR2(H134R)-EYFP-WPRE-PA (UNC Vector Core),

668 2.rAAV2/hsyn-hChR2(H134R)-mcherry-WPRE-PA (UNC Vector Core),

669 3.rAAV2-EF1α-DIO-hChR2(H134R)-EYFP (UNC Vector Core), or

670 4. ssAAV-2/2-shortCAG-dlox-hChR2(H134R)_EYFP(rev)-dlox-WPRE-hGHp(A) (VVF, Zurich).

671 We used the vector rAAV2/hsyn-mcherry (UNC Vector Core) as in our control group for the
672 intravitreal injections. To identify GABAergic neurons in the SCs, the vector rAAV5-CAG-FLEX-
673 tdTomato (400 nL, UNC Vector Core) was injected into two collicular sites in order to maximize
674 expression: 1) the rostral SCs (from bregma: anteroposterior (AP) -3.6 mm; right (R) -0.8 mm;
675 dorsoventral (DV) -1.6 mm from the surface of the skull), and 2) the caudal SCs (AP -4.2 mm; R -
676 1.8 mm; DV -1.5 mm) respectively on the same day.

677 For the rabies virus tracing, 50 nL of helper virus AAV5-EF1a-DIO-TVA-V5-t2A-RG was
678 injected into the right SCs (AP -3.9 mm; R -0.8 mm; DV -1.05 to -1.15 mm from the surface of the

679 brain) in vGAT-Cre or vGluT2-Cre mice, while taking great care to maintain viral spread to within
680 the SCs layer. Three weeks later, 150 nL of the engineered rabies virus EnvA-coated G-deleted
681 rabies virus with EGFP (EnvA-ΔG-Rb-EGFP) was injected into the same location.

682 For secondary injections, fiber optic implantations and electrophysiological recordings, two
683 to three weeks were allowed to pass after the initial injection. Viral suspensions were delivered at
684 500 nL/min and 100 nL/min for intravitreal and brain injections, respectively. A puncture was made
685 2 mm posterior to the corneal limbus using a sterile 30-gauge (G) needle after pupil dilation was
686 achieved with 0.5% Alcaine. After which 1000 nL vitreous was aspirated manually using a Hamilton
687 microliter syringe. The glass capillary was then inserted through the same puncture by using a
688 microliter syringe (1.5 mm volume) into the eye, and the tip was angled toward the vitreous humor
689 and back of the eye, taking care to avoid any damage to the retina or lens. The capillary remained
690 in the eye for 2 min in order to prevent reflux of the viral suspensions. Brain injections were
691 performed by using a digital stereotaxic frame combined with a Quintessential Stereotaxic injector
692 (Stoelting) via a glass capillary. The capillary firstly reached 0.2 mm deeper than the target location
693 to give space for the viral suspensions, then was slowly retracted to the target location to complete
694 the injections. Afterwards, the capillary was retracted by 0.2 mm again and remained in position for
695 8 min. During the injections, all the mice were kept on a heating pad at 37 °C with a subcutaneous
696 injection of buprenorphine while maintaining the eyes were moisturized with Viscotears gel.

697 **Patch electrophysiology in acute midbrain slices**

698 The animals were deeply anaesthetized by using a combination of pentobarbital injected
699 intraperitoneally. To ensure rapid cooling of the midbrain, we perfused the animals transcardially
700 with an ice-cold cutting solution, containing the following (in mM): NaCl 40, KCl 2.5, NaH_2PO_4 1.25,
701 $NaHCO_3$ 26, glucose 20, sucrose 37.5, HEPES 20, NMDG 46.5, Na L-ascorbic acid 5, $CaCl_2$ 0.5
702 and $MgCl_2$ 5 (pH 7.3 with HCl). The brain was rapidly dissected out after decapitation. Coronal
703 midbrain slices (400 μm) were prepared by using a vibratome (VT1000S, Leica, Germany) in the
704 cutting solution and incubated in the same solution at 35 °C for 12 min. The sections were
705 subsequently maintained at room temperature in recording solution that contained the following (in
706 mM): NaCl 124, KCl 2.5, NaH_2PO_4 1.25, $NaHCO_3$ 26, glucose 20, $CaCl_2$ 2 and $MgCl_2$ 1 (pH 7.3).
707 Cutting and recording solutions were continuously infused with carbogen (95% O_2 and 5% CO_2)
708 throughout the procedure.

709 Whole-cell patch clamp recordings were either performed on random neurons in the SCs of
710 wild-type mice or tdTomato-expressing neurons of vGAT-Cre mice at room temperature using
711 pCLAMP 11 (Molecular Devices, USA). Midbrain slices were continuously perfused with
712 oxygenated recording solution at a rate of 2 mL/min during recording and visualized under an
713 upright CleverScope motorized microscope (Micro Control Instruments, UK) equipped with a Dodt
714 gradient contrast system (DGC-2), an oil condenser (U-AAC, Olympus, Japan) and two
715 Chameleon3 cameras (Teledyne FLIR, USA). Whole-cell recordings were obtained under visual

716 control using a 16× (0.80 NA) water dipping objective (CFI75 LWD 16X W, Nikon, Japan) combined
717 with 2× c-mount extender (EX2C, Computar, USA) and c-mount adapters (U-TV1X-2 and U-
718 CMAD3, Olympus, Japan) with Axon MultiClamp 700B amplifier and Axon Digidata 1320A digitizer
719 (Molecular Devices, USA). Signals were sampled at 20 kHz. Pipettes used for recording were pulled
720 from borosilicate glass capillaries (article no. 1403542, Hilgenberg, Germany) by a P-97
721 Micropipette Puller (Sutter Instrument, USA). Patch pipettes (5–8 MΩ) were filled with a potassium
722 gluconate based intracellular solution contained (in mM): K D-gluconate 125, EGTA 1, KCl 10,
723 HEPES 10, ATP-Mg 4, GTP-Na 0.3, phosphocreatine 10, $CaCl_2$ 0.1 and QX314 3 (pH 7.2 with
724 KOH; 290 mOsm). Due to the long recording times (usually one hour), the access resistance was
725 evaluated every 10 min to ensure that initial values (only under ~30 MΩ were considered) did not
726 increase throughout the recording session.

727 ChR2-expressing axons of retinal ganglion cells were optically stimulated with 470 nm light
728 from a high-power collimated LED source (Mightex, Canada) connected to a digital mirror device
729 (Polygon1000, Mightex, Canada) by a 3 mm-core liquid lightguide (Newport, USA). The stimulation
730 patterns were triggered via Master-8 pulse stimulator (A.M.P.I, Israel) and designed via the software
731 PolyScan2 (Mightex, Canada). TdTomato-expressing vGAT-positive neurons in the SCs were
732 detected with 540 nm light from a high-power collimated LED source (Mightex, Canada) and an
733 RFP filter set (Olympus, Japan). The 540 nm LED was connected to a 495 nm dichroic filter cube
734 (Mightex, Canada) with the 470 nm LED during the transgenic animal experiments. Both LEDs were
735 directed via a four channel BioLED light source control module (Mightex, Canada).

736 For membrane property measurements, a series of 1000 ms negative and positive injected
737 current steps from -30 pA to +40 pA in 5 pA increments were delivered through the recording
738 electrode under current-clamped conditions to each recorded neuron.

739 **Functional receptive field mapping of individual neurons**

740 We combined whole-cell electrophysiology with a digital mirror device (DMD) based dual camera
741 system to map the receptive fields of individual neurons. Optogenetic stimulation patterns were
742 created and performed during the recordings by the DMD (Polygon1000, Mightex, Canada). The
743 16× objective combined with the 2× front tube optics (Mightex, Canada) and 0.5× single photo port
744 tube lens camera adapter (Olympus, Japan) enabled a large workable field-of-view (~1.2 × 1 mm
745 working area). With this customized visual inspection system with this dual camera approach,
746 whole-cell patch-clamp recordings were performed using the high magnification light pathway
747 whereas optostimulations patterns could be performed using the low magnification pathway that
748 enables the large field of view. All neurons were voltage-clamped at −65 and 0 mV to measure
749 excitatory postsynaptic currents (EPSCs) and inhibitory postsynaptic currents (IPSCs) respectively.
750 In most neurons, synaptic currents were also recorded at intermediate potentials (at -45 mV), when
751 recordings were sufficiently stable.

752 For control experiments, whole-field stimulation patterns were delivered by 10 Hz trains of 8
753 stimuli (5 ms duration), followed by a single test stimulus at 5 s time interval, and each trace included
754 four repetitive sweeps. For the center-surround experiments, SCs neurons were subjected to the
755 following patterns: 'GridScan', 'Center-Center', 'Surround-Surround' and 'Surround-Center'. Center
756 (C) and Surround (S) areas were determined by using the GridScan protocol, which was delivered
757 10 Hz trains of 5 light pulses of 5 ms duration in 100 non-adjacent grids arranged in a 10 × 10 spatial
758 configuration across the FOV (0.1 × 0.07 mm for each one). After the end of the GridScan, we
759 promptly calculated the maximum EPSC and IPSC amplitudes for each grid after it was normalized
760 and filtered using custom-written MATLAB (MathWorks). Excitatory postsynaptic current amplitudes
761 arising from each grid location were thresholded on the basis of their evoked amplitude. Grid
762 locations that yielded ≥ 10% of the peak EPSC amplitude for the recorded neuron, were considered
763 to be part of the center zone, whereas locations that did not pass this threshold were considered to
764 be part of the surround zone. To trigger center-surround interactions, the surround was
765 optostimulated by a single pulse that was then followed by a two or five-pulse train stimulation
766 delivered to the center. We experimented with a range of different surround stimulation durations (5,
767 20, 50 ms) and with a range of surround-center delays (0, 10, 20, 50 ms) to explore the parameter
768 space. Data was obtained using intermediate values for most of the trials, thereby also avoiding
769 technical issues or stimulation artifacts.
770
771 **Drugs used in electrophysiology**

772 Drugs were bath applied and an overall duration of at least 5 min was allowed before testing their
773 effects, which was followed by a washout phase of at least 10 minutes. Unless otherwise indicated,
774 drugs were perfused during patch-clamp recordings under the given conditions using a two-gauge
775 peristaltic pump (Pretech Instruments, Sweden). The complete list of drugs used is provided in
776 Supplementary Table 2.
777
778 **Estimation of synaptic conductances**

779 To deconvolve inhibitory and excitatory synaptic conductance, recordings were performed during
780 'center-center', 'surround-surround', 'surround-center', and 'global' optostimulation. A Cesium-based
781 QX314 solution was used in the recording pipette to improve intrinsic conductance isolation and
782 block action potential discharge conditions (Fig. 1 and Supplementary Fig. 2-3). Evoked synaptic
783 currents used in this analysis were obtained by averaging values from 5 to 10 sweeps for each
784 recorded cell. Due to the long recording times (usually one hour), the access resistance was
785 evaluated every 10 min to ensure that initial values (only under ~30 MΩ were considered) did not
786 increase throughout the recording session. This procedure was repeated for two to three different
787 potentials (−65, −45, and 0 mV) held with different levels of current injection. Customized Matlab

788 scripts were written to estimate the total, excitatory and inhibitory synaptic conductances based on
789 the equations used in Wehr and Zador (2004; *see also* Haider et al., 2015).
790

791 **Neuronal reconstruction**

792 To identify the dendritic fields from the recorded neurons, we used 0.3% Neurobiotin (Vector
793 Laboratories, no.VESP-1120-50) in the intracellular solution during whole-cell recordings. We post
794 fixed the midbrain slices and then used PBS to wash them. To visualize the neurons, we stained
795 them with streptavidin Cy5 (1:400, Jackson ImmunoResearch, no. 016-170-084) and imaged them
796 using confocal microscopy with a 20× objective (LSM-800, Zeiss, Germany). The images were
797 processed with ImageJ software, and the neurons were reconstructed by using the plugin Simple
798 Neurite tracer. The dendritic areas of each labeled neuron were calculated by tracing a convex
799 polygon around the outermost tips of the dendritic field. The SC cell types were then classified on
800 the basis of their geometry [35].

801

802 **Fiber optic implantation and cFos activation**

803 Two weeks after the intravitreal injection, a 200 μm diameter fiber optic (Thorlabs, FG200UEA) was
804 implanted into the right SCs (from bregma: AP -3.6 mm; R -1.0 mm; DV -1.0 mm from the brain
805 surface). The mice recovered for at least one week before the cFos induction experiment. The mice
806 were habituated to handling in an open field area (60 cm × 60 cm × 60 cm; W×D×H) and the
807 connected optic fiber for at least 3 days before proceeding with the experiment. To minimize stress,
808 bedding from the cage was placed in the box. Optogenetic stimulation was not initiated for 90 min
809 after the mice were placed in the dark box to avoid any prior visual effects on the observed cFos
810 expression. The RGC axonal terminals in the SCs were stimulated with a train of 1 s square pulses
811 of 40 Hz frequency (10 ms ON and 15 ms OFF) every 10 sec for a total of 40 min. After the
812 stimulation period, the mice were left undisturbed for 60-70 min to ensure sufficient cFos protein
813 expression. A maximum of 90 min after the end of the stimulation period was allowed before the
814 mice were euthanized with pentobarbital and perfused with ice-cold 4% paraformaldehyde (PFA) in
815 0.01 M (1×) phosphate-buffered saline (PBS) buffer. The brain and retinas were subsequently
816 dissected, and post fixed in 4% PFA overnight at 4°C.

817

818 **Immunofluorescent staining and *in situ* hybridization**

819 Mice were anesthetized by pentobarbital and perfused with 1× PBS and 4% PFA. The brains (and
820 eyes, to confirm pan-retina transfection) were harvested and fixed in PFA at 4 °C overnight, then
821 washed with PBS for 3 times. The brain was placed in 15% sucrose solution for 24 h, then
822 transferred into 30% sucrose solution for 24–72 h. The brains were subsequently embedded in

823 optimal cutting temperature compound (OCT), frozen with dry ice and kept at -20 °C for short-term
824 storage. The cryostat sectioning was performed on a Epredia NX70 cryostat. The brains, between
825 the thalamus and brainstem, were sectioned in 14 μm thickness, about 80% (12 to 15) sections in
826 the SCs were collected on glass slides, and every 6th section was sampled for the following staining
827 (the interval is about 0.105 mm). The other parts of the brain were sectioned in 40 μm thickness
828 and stored in 1× PBS with 0.01% sodium azide.

829 The fluorescence *in situ* hybridization was performed with RNAscope Multiplex Fluorescent
830 Reagent Kit v2 (ACD, Cat. No. 323100). The probes for vGluT2 (Mm-Slc17a6-C2, ACD, Cat. No.
831 319171-C2) and vGAT (Mm-Slc32a1, ACD, Cat. No. 319191) were used to identify the cell types.
832 The manufacturer's protocol was followed. Co-staining of vGAT and vGluT2 *in situ* hybridizations
833 was also performed for control experiment, and the results were shown in Supplementary Fig. 5.

834 Immediately following the *in situ* hybridization, the brain sections were incubated in chicken
835 anti-V5 primary antibody (Abcam, ab9113) in 1:750 at room temperature overnight, then washed
836 with 1× TBST (0.3% TritonX-100), and incubated in donkey anti-chicken Cy3 secondary antibody
837 (Jackson ImmunoResearch, no. 703-165-155) in 1:1000. All the antibodies were diluted with 1×
838 TBST (0.3% TritonX-100, 3% BSA, 0.01% sodium azide). After PBS washing and DAPI staining,
839 the sections were mounted with an antifade mounting medium (VWR, BSBT AR1109). For the cFos
840 staining, rat or rabbit anti-cFos primary antibodies (Synaptic Systems, no. 226-017 or no. 226-003,
841 1:500) and GABA primary antibody (Sigma-Aldrich, A2052, 1:2000) were used in 1× PBST (0.3%
842 TritonX-100, 5% donkey serum, 0.01% sodium azide) at room temperature overnight, then the
843 sections were stained with Cy3 donkey anti-rabbit (Jackson ImmunoResearch, no. 711-165-152) or
844 AF647 donkey anti-rat (Jackson ImmunoResearch, no. 712-605-153). The same following steps
845 are previously described.

846

847 The retinas were first removed from the eye in the perfused animals and then flattened with
848 the help of four incisions, and finally washed in 1x PBS for 3 times. For the retina immunostaining,
849 the retina was first treated with pre-heated (about 70 °C) 1× antigen retrieval citrate buffer (Sigma,
850 C9999), then followed the same protocol as with the brain section described above. Rabbit anti-S-
851 opsin primary antibody (Sigma, AB5407) and donkey anti-rabbit Cy3 secondary antibody were both
852 used in 1:1000 to visualize the short-wave photoreceptors, which reveals retinal orientation.

853

854 **Network model**

855 We used an integrate and fire model to simulate the dynamics of neurons. The subthreshold
856 membrane potential (V_m) of each neurons was described by the following differential equation:

857 $$C_m dV_m/dt = g_L (V_m - E_L) + I^{bkg}_{syn} + I^{net}_{syn} + I^{stim}_{syn},$$

where C_m is the membrane capacitance, g_L is the leak conductance, I^{net}_{syn} is the total synaptic input from neurons within the network, I^{bkg}_{syn} is the background input from other networks, I^{stim}_{syn} is input corresponding to center or surround inputs (*see* Supplementary Table 3). When the membrane potential reached V_{th}, spike was elicited and the V_m was reset to E_L for t_{ref} millisecond. In the network all neurons were identical. Neuron parameters are provided in Supplementary Table 4.

Synaptic inputs were modelled as conductance transients with following dynamics:

$$g_{syn} = J_{syn}t/tau_{syn}\ exp(-(t-(t_{spk}+ d_{syn}))/tau)\ when\ t-t_{spk} >0\ else\ g_{syn} = 0,$$

where t_{spk} is the spike time, d_{syn} is the synaptic delay, J_{syn} *{syn: ee, ei, ie, ii, ex, ix)* is the amplitude of the postsynaptic potential (PSP), and tau_{syn} is the synaptic time constant. In our model all synapses of a particular type (external, excitatory, or inhibitory) have the same parameters (*see* Supplementary Table 5). In our model we fixed the amplitude (J_{syn}) of the external excitatory (J_{ex}), inhibitory (J_{ix}) synapses and J_{ii} (inh. → inh.). The value of J_{ee} (exc. → exc.), J_{ei} (exc. → inh.), and J_{ie} (inh. → exc.) were systematically varied. Synapse parameters are provided in Supplementary Table 5.

We considered a network with 6400 excitatory and 6400 inhibitory neurons. Neurons were placed on an 80 × 80 grid. Because we have the same population size for the two neuron types, both types of neurons were placed on the same size grid. Neurons were connected based on their spatial distance. To avoid boundary effects, the 80 × 80 grid was folded as a torus. The connection probability decreased as a function of distance according to a Gaussian function. The standard deviation of the Gaussian was set to 16 and 20 for excitatory and inhibitory synapses, respectively. This was based on our experimental data which showed that inhibitory neurons have a slightly bigger extent of their spatial connectivity than that of excitatory synapses (Fig. 2f). 16 and 20 grid points constitute 2% and 2.5% of our network space. The area of the Gaussian function (*i.e.* the total number of connections sent out by a neuron) was decided based on the input convergence we measured in our experiments (Fig. 2g-h). Network connectivity parameters are provided in Supplementary Table 6.

Each neuron received Poisson type excitatory and inhibitory spiking inputs to mimic inputs from outside the network and to obtain a low firing rate (< 1 Hz) background activity. *See* Supplementary Table 7 for parameters.

To model a short flash like input to the center region, we selected 314 excitatory and 314 inhibitory neurons, located in a circle (radius = 10 grid points) at the center of our network model. These neurons received a single synchronous spike from 10 presynaptic neurons (from the retina). Each spike elicited 1.1 mV depolarization. Each neuron received such a synchronous spike event at the stimulus onset (*Tcenter*). Each individual neuron received the synchronous spike event at a time *Tcenter* + *r,* where *r* is a random number drawn from a uniform distribution (U[0,1]). Center stimulus was presented to the neurons in three conditions: center only, center stimulus just at the

894 end of the surround stimulus (*see* below) and center while the surround stimulus was still on. *See*
895 Supplementary Table 3 for more details.

896 To mimic the surround stimulus, we selected 3286 E-neurons and 3286 I-neurons from a
897 square region in the network with a side of 60 grid points. The center neurons (see above) were
898 located at the center of this square. For the surround stimulus we excluded the center neurons. The
899 surround stimulus was injected in the selected neurons in the form of uncorrelated Poisson type
900 spike trains. See Supplementary Table 3 for more details.

901 The network model was simulated using the simulator NEST [54].

902 **Statistical analysis and data plotting**

903 For each mouse, 10–16 sections were stained and visualized. Confocal images (20×) were used
904 for the manual scoring of co-expression of vGAT/vGluT2, V5 and RV-GFP. Whole-brain images
905 (10×) were acquired with a fluorescent microscope (Leica DM6000B) and a digital camera
906 (Hamamatsu Orca-FLASH 4.0 C11440). They were manually registered to a bregma AP coordinate
907 (from bregma -3.2 to -4.9), and subsequently aligned to the Allen Reference Atlas with the
908 WholeBrain R package [37,55]. Every detected Rb-EGFP positive neuron was registered, and the
909 coordinates were used for the following analysis. As the main source of monosynaptic input and
910 local input, only the RV-GFP positive cells in the SCs were included in the calculation. For the
911 comparison between mice, the number of input neurons were normalized to the total number of
912 detected Rb-EGFP positive neurons in SCs. All the density estimations were done using a Gaussian
913 kernel and were then plotted in R.

914 To minimize the effects of M-L differences of the injection sites between animals, the
915 centroid of the starter neurons was first computed using k-means clustering analysis, which then
916 allowed us to plot the relative M-L coordinate for each neuron. As for the depth estimation, the
917 coordinates of the SC surface were first obtained with the WholeBrain R package, then the depth
918 of each neuron was calculated after subtracting the difference. In both, M-L and depth density plots,
919 only 3 central brain sections with the highest starter density were included according to the AP
920 density plot.

921 After confocal imaging the cFos fluorescence was quantified by a 3d object counter plug-in
922 of Fiji. Colocalized cFos+ and GABA+ cells were manually counted in three areas in SCs (C, SM
923 and SL; *see* Fig. 4). The statistical analysis and visualization were done in Python (code available
924 upon request).

925 We used three model stimulation protocols: center only (center), center stimulus just at the
926 end of the surround stimulus (center after surround) and center while the surround stimulus was
927 still on (center with surround). Each paradigm was repeated 20 times. For each stimulus
928 presentation, we recorded excitatory conductance from a single neuron. We estimated the across

929 trial mean and variance of the conductance input to the recorded neuron. Finally, the results were
930 rendered as the mean and variance of the excitatory conductance at specific time points after the
931 onset of the stimulus in all three stimulus paradigms. In addition, we recorded spiking activity from
932 all the neurons and estimated the firing rate of neurons. The network model was simulated using
933 the simulator NEST. All differential equations were integrated using Runga-Kutta method with a
934 time step of 0.1 ms.

935 Electrophysiology data analyses were performed using Clampfit 11 (Molecular Devices,
936 USA), GraphPad Prism (GraphPad Software 7.00, USA), ImageJ (1.53c, NIH, USA), RStudio (R
937 3.6.1) or MATLAB (R2018b, MathWorks, USA). Data were all presented as mean values ± s.e.m.
938 Before performing paired *t*-test or one-way ANOVA analysis, the normality and the homogeneity of
939 variance were first evaluated using Kolmogorov–Smirnov's test and Brown–Forsythe's test. If the *p*
940 value of Kolmogorov–Smirnov's test was less than 0.05, Wilcoxon's signed-rank test would be used
941 instead of paired *t*-test. If *p* value of Brown–Forsythe's test was less than 0.05, Friedman test and
942 Kruskal–Wallis test would be used instead of a repeated-measures one-way ANOVA (RM one-way
943 ANOVA) and ordinary one-way ANOVA, respectively. *p* values were corrected for deviation using
944 the Geisser–Greenhouse correction. Once the *p* value of a one-way ANOVA analysis was less than
945 0.05, Tukey's multiple comparisons test would be performed. *F* and df (df1, df2) are degrees of
946 freedom for one-way ANOVA and paired *t*-test, respectively. *p* values less than 0.05 were
947 considered significant with asterisks in figures denoting as follows: *$p < 0.05$, **$p < 0.01$, ***$P <$
948 0.001, ****$p < 0.0001$, *ns*, no significance.

949

950

951

952 **Supplementary Table 1. Viruses used in this study**

Name	Type	Titer	Source
rAAV2/hsyn-hChR2(H134R)-EYFP-WPRE-PA	AAV2	5.6×10^{12} vg/mL	UNC Vector Core
rAAV2/hsyn-hChR2(H134R)-mcherry-WPRE-PA	AAV2	5.1×10^{12} vg/mL	UNC Vector Core
rAAV2-EF1α-DIO-hChR2(H134R)-EYFP	AAV2	4.4×10^{12} vg/mL	UNC Vector Core

ssAAV-2/2-shortCAG-dlox-hChR2(H134R)_EYFP(rev)-dlox-WPRE-hGHp(A)	AAV2	1.4 x 10^{12} vg/mL	ZNZ Viral Vector Facility
rAAV2/hsyn-mcherry	AAV2	5.3 × 10^{12} vg/mL	UNC Vector Core
rAAV5-CAG-FLEX-tdTomato	AAV5	7.8 × 10^{12} vg/mL	UNC Vector Core
AAV5-EF1a-DIO-TVA-V5-t2A-RG	AAV5	1.2 × 10^{12} vg/mL	DMC laboratory
EnvA-ΔG-Rb-EGFP	Modified Rabies	1 × 10^{10} vg/mL	DMC laboratory

953

954 **Supplementary Table 2. Drugs used in electrophysiology experiments**

Compound	Drug name	Concentration	Source
Gabazine (SR 95531)	6-Imino-3-(4-methoxyphenyl)-1(6*H*)-pyridazinebutanoic acid hydrobromide	10 μM	Tocris Bioscience, USA
TTX	(4*R*,4a*R*,5*R*,7*S*,9*S*,10*S*,10a*R*,11*S*,12*S*)-Octahydro-12-(hydroxymethyl)-2-imino-5,9:7,10a-dimethano-10a*H*-[1,3]dioxocino[6,5-*d*]pyrimidine-4,7,10,11,12-pentol	1 μM	Tocris Bioscience, USA
4-AP	4-Aminopyridine	100 μM	Sigma-Aldrich
QX314	*N*-(2,6-Dimethylphenylcarbamoylmethyl)triethylammonium bromide	3 mM	Tocris Bioscience, USA

955

956

957

958

959

960 **Supplementary Table 3. Stimulus input**

Type of input	Stimulated neurons	Spike input	Stimulus PSP	Repeats
Center Input	All neurons (exc. and inh.) in a circle with radius 10 grid points. 314 exc. neurons and 314 inh. neurons.	Each neuron received 10 synchronous spikes corresponding to the presentation of a flash like center stimulus. Arrival time of each synchronous spike event was taken from a uniform distribution U[0,1] ms.	1.03 mV at -54 mV to exc. neurons 0.86 mV at -54 mV to exc. neurons	20
Surround input	All neurons (exc. and inh.) within a square of size 60 grid point centered at the center of the network. Neurons part of the center stimulus were excluded. 3286 exc. neurons and 3286 inh. neurons.	Poisson type spiking input with a spike rate of 100 Hz. Surround stimulus was presented for 200 ms.	2.58 mV at -54 mV	20
Surround input	All neurons (exc. and inh.) within a square of size 60 grid point centered at the center of the network. Neurons part of the center stimulus were excluded. 3286 exc. neurons and 3286 inh. neurons.	Poisson type spiking input with a spike rate of 50:10:130 Hz. Surround stimulus was presented for 200 ms.	2.58 mV at -54 mV	20

961

962

963

964

965 **Supplementary Table 4. Neuron parameters**

Parameter	Value	Description
C_m	200 pF	Membrane capacitance
g_L	20 nS	Leak conductance
V_{th}	-54 mV	Spike threshold
E_L	-70 mV	Reversal potential for leak conductance
t_{ref}	2 ms	Refractory time

966

967

968 **Supplementary Table 5. Synapse parameters**

Parameter	Value	Description	Notes
J_{ex}	0.63 mV	EPSP amplitude for connection from external excitatory inputs	EPSP amplitude was measured at a holding potential of -54 mV
J_{ix}	-0.3 mV	IPSP amplitude for connection from external inhibitory inputs	IPSP amplitude was measured at a holding potential of -54 mV
J_{ee}	{0.13, 0.26} mV	EPSP amplitude for exc. → exc. connection	EPSP amplitude was measured at a holding potential of -54 mV
J_{ei}	{0.11, 0.21, 0.32, 0.42, 0.53, 0.63} mV	EPSP amplitude for exc. → inh. connection	EPSP amplitude was measured at a holding potential of -54 mV
J_{ie}	{-0.14, -0.17, -0.19, -0.22, -0.28, -0.3} mV	IPSP amplitude for inh. → exc. connection	IPSP amplitude was measured at a holding potential of -54 mV
J_{ii}	0.055 mV	IPSP amplitude for inh. → inh. connection	IPSP amplitude was measured at a holding potential of -54 mV
tau_e	1.0 ms	Time constant of excitatory synapses	This was the same for both exc. → exc., exc. → inh. synapses and external excitatory input synapses

tau_i	3.0 ms	Time constant of inhibitory synapses	This was the same for both inh. → exc., inh. → inh. synapses and external inhibitory input synapses
d_{ee}	0.2 ms	Synaptic delay for exc. → exc. synapses	
d_{ei}	0.1 ms	Synaptic delay for exc. → inh. synapses	
d_{ie}	0.1 ms	Synaptic delay for inh. → exc. synapses	
d_{ii}	0.1 ms	Synaptic delay for inh. → inh. synapses	

Supplementary Table 6. Network connectivity

Parameter	Value	Description	Notes
N_e	6400	Excitatory neurons	
N_i	6400	Inhibitory neurons	
Excitatory grid size	80 × 80	Neurons were placed on a regular grid	
Inhibitory grid size	80 × 80	Neurons were placed on a regular grid	
C_{ee}	0.135	Connection probability between exc. to exc. neurons. This number refers to the integral of the connectivity kernel	Based on our experimental data (*See* Fig. 2g)
C_{ei}	0.112	Connection probability between exc. to inh neurons. This number refers to the integral of the connectivity kernel	Based on our experimental data (*See* Fig. 2g)
C_{ie}	0.315	Connection probability between inh to exc. neurons. This number refers to the integral of the connectivity kernel	Based on our experimental data (*See* Fig. 2g)
C_{ii}	0.3375	Connection probability between inh. to inh. neurons. This number refers to the integral of the connectivity kernel	Based on our experimental data (*See* Fig. 2g)
S_e	16 grid points 2% of the network size	Standard deviation of Gaussian used to estimate distance dependent connectivity from exc. to exc. and exc. to inh. neurons.	

S_i	20 grid points 2.5% of the network size	Standard deviation of Gaussian used to estimate distance dependent connectivity from inh. to exc. and inh. to inh. neurons.	

Supplementary Table 7. External Input

Parameter	Value	Description
nu_exc	1000 Hz	Poisson type spike trains were injected in all neurons
nu_inh	600 Hz	Poisson type spike trains were injected in all neurons

Data and code availability

Any additional information required to reanalyze the data reported in this paper is available from the lead contact upon request. Data reported in this paper and all original code are available and will be shared by the lead contact upon request.

REFERENCES

1. Churchland, P. S. & Sejnowski, T. J. Neural Representation and Neural Computation. *Philos. Perspect.* **4**, 343–382 (1990).
2. Grossberg, S. The quantized geometry of visual space: The coherent computation of depth, form, and lightness. *Behav. Brain Sci.* **6**, 625–657 (1983).
3. Angelucci, A. *et al.* Circuits and Mechanisms for Surround Modulation in Visual Cortex. *Annu. Rev. Neurosci.* **40**, 425–451 (2017).
4. Knudsen, E. I. & Konishi, M. Center-Surround Organization of Auditory Receptive Fields in the Owl. *Science* **202**, 778–780 (1978).
5. Sachdev, R., Krause, M. & Mazer, J. Surround suppression and sparse coding in visual and barrel cortices. *Front. Neural Circuits* **6**, (2012).
6. Olsen, S. R. & Wilson, R. I. Lateral presynaptic inhibition mediates gain control in an olfactory circuit. *Nature* **452**, 956–960 (2008).

995 7. Hubel, D. H. & Wiesel, T. N. Receptive fields of single neurones in the cat's striate cortex. *J.*
996 *Physiol.* **148**, 574–591 (1959).
997 8. Schiller, P. H. & Koerner, F. Discharge characteristics of single units in superior colliculus of
998 the alert rhesus monkey. *J. Neurophysiol.* **34**, 920–936 (1971).
999 9. Kardamakis, A. A., Saitoh, K. & Grillner, S. Tectal microcircuit generating visual selection
1000 commands on gaze-controlling neurons. *Proc. Natl. Acad. Sci.* **112**, E1956–E1965 (2015).
1001 10. Kasai, M. & Isa, T. Imaging population dynamics of surround suppression in the superior
1002 colliculus. *Eur. J. Neurosci.* **44**, 2543–2556 (2016).
1003 11. McIlwain, J. T. & Buser, P. Receptive fields of single cells in the cat's superior colliculus. *Exp.*
1004 *Brain Res.* **5**, 314–325 (1968).
1005 12. Schiller, P. H. & Stryker, M. Single-unit recording and stimulation in superior colliculus of the
1006 alert rhesus monkey. *J. Neurophysiol.* **35**, 915–924 (1972).
1007 13. Bonin, V., Mante, V. & Carandini, M. The Suppressive Field of Neurons in Lateral Geniculate
1008 Nucleus. *J. Neurosci.* **25**, 10844–10856 (2005).
1009 14. Jones, H. E., Grieve, K. L., Wang, W. & Sillito, A. M. Surround suppression in primate V1. *J.*
1010 *Neurophysiol.* **86**, 2011–2028 (2001).
1011 15. Born, R. T. & Bradley, D. C. Structure and Function of Visual Area Mt. *Annu. Rev. Neurosci.*
1012 **28**, 157–189 (2005).
1013 16. Fernandes, A. M. *et al.* Neural circuitry for stimulus selection in the zebrafish visual system.
1014 *Neuron* **109**, 805-822.e6 (2021).
1015 17. Kardamakis, A. A., Pérez-Fernández, J. & Grillner, S. Spatiotemporal interplay between
1016 multisensory excitation and recruited inhibition in the lamprey optic tectum. *eLife* **5**, e16472
1017 (2016).
1018 18. Flores-Herr, N., Protti, D. A. & Wässle, H. Synaptic currents generating the inhibitory surround
1019 of ganglion cells in the mammalian retina. *J. Neurosci. Off. J. Soc. Neurosci.* **21**, 4852–4863
1020 (2001).

1021 19. Kim, Y. J. *et al.* Origins of direction selectivity in the primate retina. *Nat. Commun.* **13**, 2862
1022 (2022).
1023 20. Solomon, S. G., Lee, B. B. & Sun, H. Suppressive Surrounds and Contrast Gain in
1024 Magnocellular-Pathway Retinal Ganglion Cells of Macaque. *J. Neurosci.* **26**, 8715–8726
1025 (2006).
1026 21. Zhang, Y., Kim, I.-J., Sanes, J. R. & Meister, M. The most numerous ganglion cell type of the
1027 mouse retina is a selective feature detector. *Proc. Natl. Acad. Sci.* **109**, E2391–E2398 (2012).
1028 22. Carandini, M. & Heeger, D. J. Normalization as a canonical neural computation. *Nat. Rev.*
1029 *Neurosci.* **13**, 51–62 (2012).
1030 23. Sato, T. K., Haider, B., Häusser, M. & Carandini, M. An excitatory basis for divisive
1031 normalization in visual cortex. *Nat. Neurosci.* **19**, 568–570 (2016).
1032 24. Veale, R., Hafed, Z. M. & Yoshida, M. How is visual salience computed in the brain? Insights
1033 from behaviour, neurobiology and modelling. *Philos. Trans. R. Soc. B Biol. Sci.* **372**, 20160113
1034 (2017).
1035 25. Zhang, X., Zhaoping, L., Zhou, T. & Fang, F. Neural Activities in V1 Create a Bottom-Up
1036 Saliency Map. *Neuron* **73**, 183–192 (2012).
1037 26. Zhaoping, L. From the optic tectum to the primary visual cortex: migration through evolution of
1038 the saliency map for exogenous attentional guidance. *Curr. Opin. Neurobiol.* **40**, 94–102
1039 (2016).
1040 27. Ahmadlou, M., Tafreshiha, A. & Heimel, J. A. Visual Cortex Limits Pop-Out in the Superior
1041 Colliculus of Awake Mice. *Cereb. Cortex* **27**, 5772–5783 (2017).
1042 28. McPeek, R. M. & Keller, E. L. Deficits in saccade target selection after inactivation of superior
1043 colliculus. *Nat. Neurosci.* **7**, 757–763 (2004).
1044 29. Wang, L., Herman, J. P. & Krauzlis, R. J. Neuronal modulation in the mouse superior colliculus
1045 during covert visual selective attention. *Sci. Rep.* **12**, 2482 (2022).

1046 30. Wang, L. & Krauzlis, R. J. Visual Selective Attention in Mice. *Curr. Biol.* **28**, 676-685.e4
1047 (2018).
1048 31. McLaughlin, T. & O'Leary, D. D. M. Molecular gradients and development of retinotopic
1049 maps. *Annu. Rev. Neurosci.* **28**, 327–355 (2005).
1050 32. Phongphanphanee, P. *et al.* Distinct local circuit properties of the superficial and intermediate
1051 layers of the rodent superior colliculus. *Eur. J. Neurosci.* **40**, 2329–2343 (2014).
1052 33. Haider, B., Häusser, M. & Carandini, M. Inhibition dominates sensory responses in the awake
1053 cortex. *Nature* **493**, 97–100 (2013).
1054 34. Wehr, M. & Zador, A. M. Balanced inhibition underlies tuning and sharpens spike timing in
1055 auditory cortex. *Nature* **426**, 442–446 (2003).
1056 35. Gale, S. D. & Murphy, G. J. Distinct Representation and Distribution of Visual Information by
1057 Specific Cell Types in Mouse Superficial Superior Colliculus. *J. Neurosci.* **34**, 13458–13471
1058 (2014).
1059 36. Liu, Y. *et al.* Mapping visual functions onto molecular cell types in the mouse superior
1060 colliculus. *Neuron* **111**, 1876-1886.e5 (2023).
1061 37. Ährlund-Richter, S. *et al.* A whole-brain atlas of monosynaptic input targeting four different
1062 cell types in the medial prefrontal cortex of the mouse. *Nat. Neurosci.* **22**, 657–668 (2019).
1063 38. Lazaridis, I. *et al.* A hypothalamus-habenula circuit controls aversion. *Mol. Psychiatry* **24**,
1064 1351–1368 (2019).
1065 39. Wickersham, I. R. *et al.* Monosynaptic restriction of transsynaptic tracing from single,
1066 genetically targeted neurons. *Neuron* **53**, 639–647 (2007).
1067 40. Reinhard, K. *et al.* A projection specific logic to sampling visual inputs in mouse superior
1068 colliculus. *eLife* **8**, e50697 (2019).
1069 41. Gehr, C., Sibille, J. & Kremkow, J. Retinal input integration in excitatory and inhibitory
1070 neurons in the mouse superior colliculus in vivo. 2023.04.07.536092 Preprint at
1071 https://doi.org/10.1101/2023.04.07.536092 (2023).

1072 42. Hong, Y. K., Kim, I.-J. & Sanes, J. R. Stereotyped axonal arbors of retinal ganglion cell subsets
1073 in the mouse superior colliculus. *J. Comp. Neurol.* **519**, 1691–1711 (2011).
1074 43. Niell, C. M. & Scanziani, M. How Cortical Circuits Implement Cortical Computations: Mouse
1075 Visual Cortex as a Model. *Annu. Rev. Neurosci.* **44**, 517–546 (2021).
1076 44. Adesnik, H., Bruns, W., Taniguchi, H., Huang, Z. J. & Scanziani, M. A neural circuit for spatial
1077 summation in visual cortex. *Nature* **490**, 226–231 (2012).
1078 45. O'Rawe, J. F. *et al.* Excitation creates a distributed pattern of cortical suppression due to varied
1079 recurrent input. *Neuron* (2023) doi:10.1016/j.neuron.2023.09.010.
1080 46. Douglas, R. J., Koch, C., Mahowald, M., Martin, K. A. & Suarez, H. H. Recurrent excitation in
1081 neocortical circuits. *Science* **269**, 981–985 (1995).
1082 47. Harris, K. D. & Mrsic-Flogel, T. D. Cortical connectivity and sensory coding. *Nature* **503**, 51–
1083 58 (2013).
1084 48. Guo, L. & Kumar, A. Role of interneuron subtypes in controlling trial-by-trial output variability
1085 in the neocortex. *Commun. Biol.* **6**, 1–13 (2023).
1086 49. Baden, T. *et al.* The functional diversity of retinal ganglion cells in the mouse. *Nature* **529**,
1087 345–350 (2016).
1088 50. Kapadia, M. K., Ito, M., Gilbert, C. D. & Westheimer, G. Improvement in visual sensitivity by
1089 changes in local context: parallel studies in human observers and in V1 of alert monkeys.
1090 *Neuron* **15**, 843–856 (1995).
1091 51. Krieger, B., Qiao, M., Rousso, D. L., Sanes, J. R. & Meister, M. Four alpha ganglion cell types
1092 in mouse retina: Function, structure, and molecular signatures. *PLoS ONE* **12**, e0180091 (2017).
1093 52. Brenner, J. M., Beltramo, R., Gerfen, C. R., Ruediger, S. & Scanziani, M. A genetically defined
1094 tecto-thalamic pathway drives a system of superior-colliculus-dependent visual cortices.
1095 *Neuron* **111**, 2247-2257.e7 (2023).
1096 53. Zénon, A. & Krauzlis, R. J. Attention deficits without cortical neuronal deficits. *Nature* **489**,
1097 434–437 (2012).

54. Fardet, T. *et al.* NEST 2.20.0. (2020) doi:10.5281/zenodo.3605514.

55. Fürth, D. *et al.* An interactive framework for whole-brain maps at cellular resolution. *Nat. Neurosci.* **21**, 139–149 (2018).

SUPPLEMENTARY FIGURES AND FIGURE LEGENDS (S1-S7)

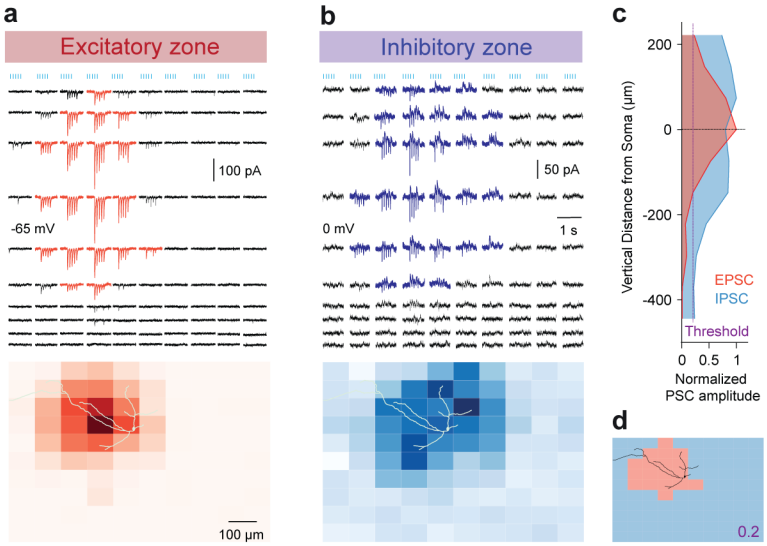

Fig. S1: Mapping excitatory and inhibitory zones of SCs neurons

(a-b) A wide-field (WF) SCs neuron responding with the neuron responding with excitatory and inhibitory postsynaptic currents (EPSCs measured at -65 mV shown in **a**; IPSCs measured at 0 mV shown in **b**) in response to a 20 Hz 5-light-pulse train delivered pseudo-randomly as a 120×100 µm grid optostimulation. Bottom panels: Response maps superimposed with the reconstructed morphology of the intracellularly stained WF neuron with Neurobiotin during whole-cell recording. Heat maps with darker shades coding for stronger responses in amplitudes.

(c) Distance from soma as a function of normalized postsynaptic amplitude. Red for excitatory; Blue for inhibitory. Vertical dashed line indicates threshold applied at a normalized value of 0.2.

(d) Center and surround zone of the WF zone determined by following thresholding approach applied to the excitatory PSCs shown in **(c)**. Areas occupying a larger value compared to threshold are considered to be part of the center zone.

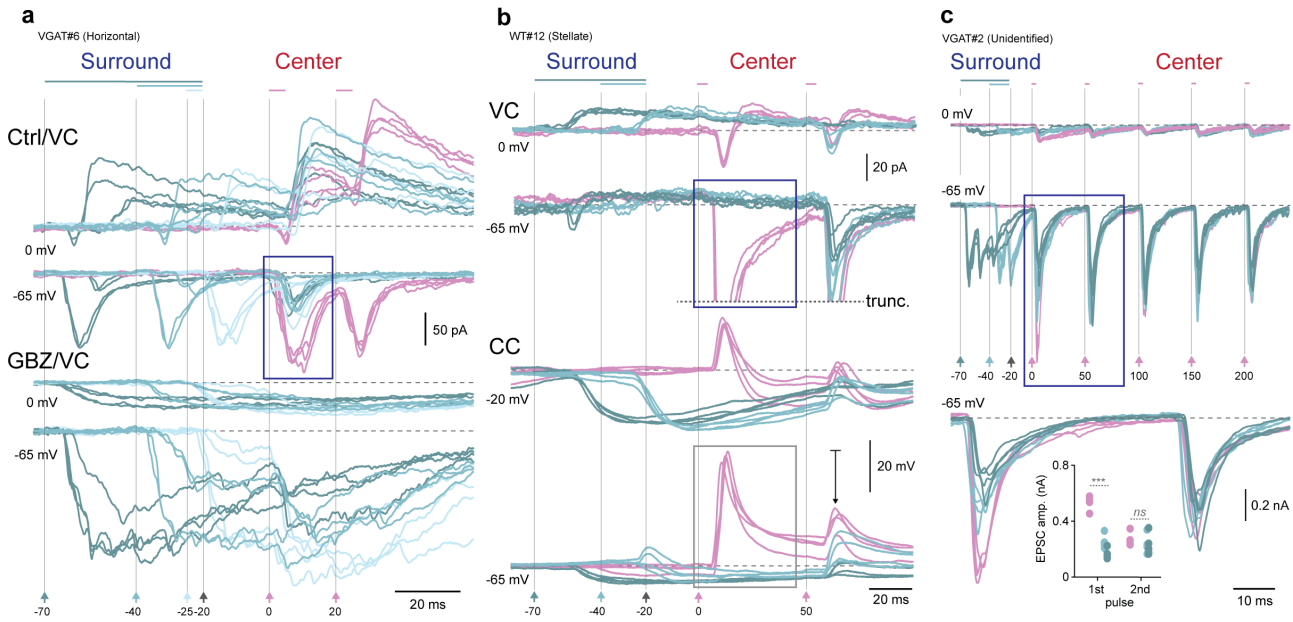

Fig. S2: Three different examples of synaptic modulation between center and surround zones. **(a)** Top: Individual current traces held at reverse potentials for chloride-mediated GABAergic inhibition (-65 mV) and glutamate-mediated ionotropic excitation (0 mV) that span continuously surround and center optostimulation of the neuron (2 pulses separated by 20 ms) shown in Fig. 1d. Here, surround network activation can be seen to effectively reduce the center EPSC amplitudes (blue rectangle) when comparing to center only responses (in magenta). Evoked responses to surround stimulation of all durations (5, 20 and 50 ms; shades of green) are also seen to drive bistable excitatory and inhibitory responses. (Bottom) Voltage-clamp (VC) recordings in response to surround optostimulation after bath application of 10 μM Gabazine (GBZ), thereby removing the effect of GABAergic inhibition. Same color-coding scheme as in Fig. 1. Time stamps are centered around the onset of the first center pulse.
(b) (Top) Synaptic current recordings performed in voltage clamp of a stellate neuron shown in Fig. 1e that is subject to the 20 Hz optostimulation (2 pulses). Center EPSCs shown in the rectangle are truncated (dotted line). (Bottom) Same neuron recorded in current clamp (CC) reveals the shunting effect that surround activation has on center responses (gray rectangle) when recording at -65 mV and at a depolarized membrane potential of -20 mV. This is attributed to chloride current triggered by the surround (revealed when held at 0 mV in VC; top traces).
(c) Current traces from a vGAT+ SCs neuron in response to 20 Hz optostimulation (5 center pulses) that shows signs of surround suppression without the direct effect of synaptic inhibition. Top and middle traces: Current recordings performed at -65 mV and 0 mV reveals that this neuron does not receive direct inhibition from the surround yet its center response is attenuated suggesting that it receives less excitatory input. Bottom: Enlarged view of current traces found in blue rectangle in middle panel focusing on first and second paired pulse center stimulations. Surround stimulation has a significant effect on the first center pulse by reducing its amplitude by 50% (***, $p < 0.0001$; Student's *t*-test).

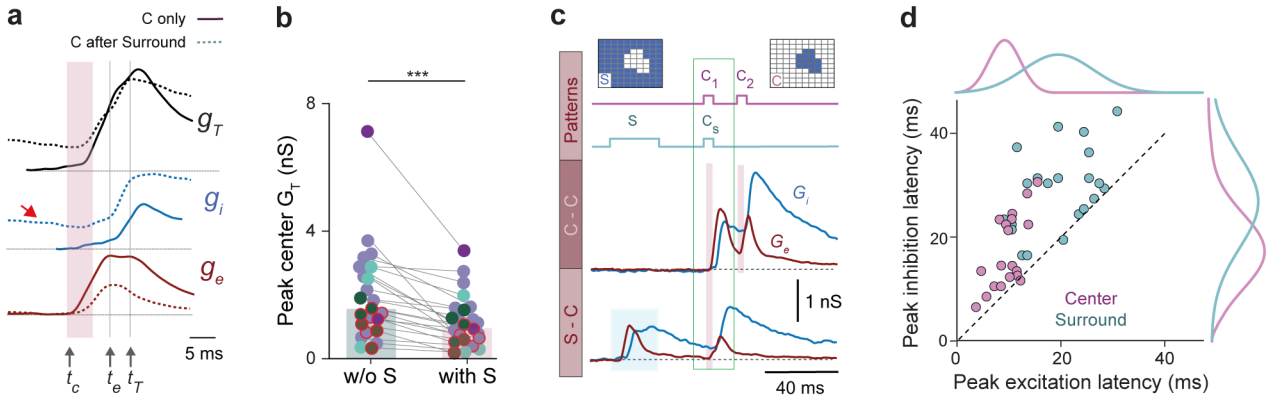

Fig. S3: Center-surround dynamics are defined by transient excitatory and inhibitory conductances.

(a) Total synaptic conductance (G_T, black line) triggered by center only (C_1) and surround-center (C_s) conditions is decomposed into excitatory (G_e, red) and inhibitory (G_i, blue) conductances. Conductances belong to recording shown in Fig. 1f, which are estimated by Wehr and Zador (2003) by using synaptic current recordings performed at -65 mV and 0 mV. Time stamps t_c, t_e and t_T symbolize the time onset for center stimulation, the time instant when peak excitation and maximal total conductance is reached, respectively. Solid lines are with center only condition and dashed lines are when center follows surround optostimulation. Red arrow indicates non-zero inhibitory conductance evoked by surround network activation at the time of t_c.

(b) Comparison of total synaptic conductance G_T between C_1 and C_s conditions. Corresponding excitatory and inhibitory conductances at peak G_T are shown in Fig. 1g-h. Color coding corresponds to morphologically or genetically identified SCs neuron cell-types (*see* Fig. 1g).

(c) Full time course of excitatory and inhibitory conductance during both stimulation conditions, C_1 and C_s. *Legends:* C-C (paired pulse center optostimulation) and S-C refers to surround followed by center optostimulation after a 20 ms refractory period.

(d) Latency to peak inhibition as a function of latency to peak excitation. On average, when comparing the center (magenta) and surround (cyan) conditions, it appears that there is an approximately 20 ms delay. This suggests that the signals originating from the surround region interact with the center responses with this time difference. Curves are a gaussian probability distribution function fitted to the data points.

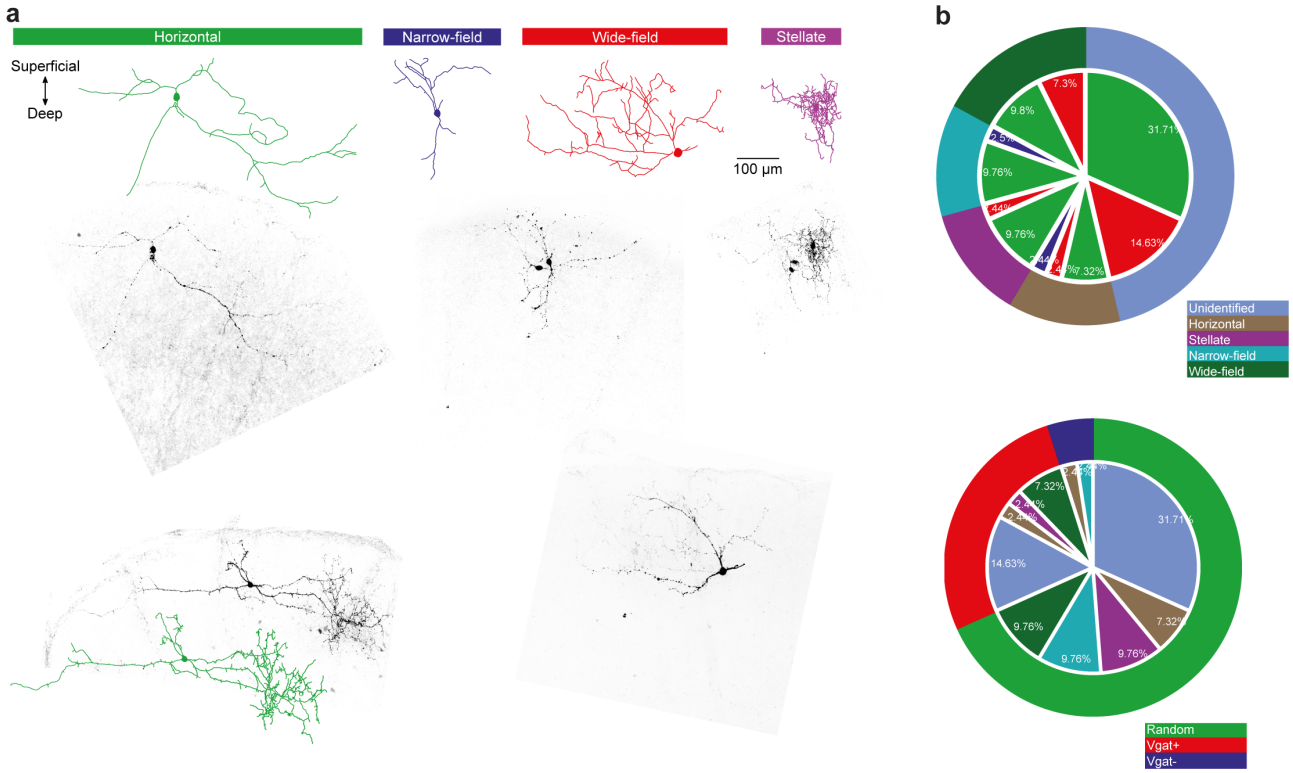

c

Morphology		100.00%	Genotype	41	500.00%	
	41	41		41	41	100.00%
Un-identified	19	46.34%	Random	13	68.42%	31.71%
			Vgat+	6	31.58%	14.63%
			Vgat-	0	0.00%	0.00%
Horizontal	5	12.20%	Random	3	60.00%	7.32%
			Vgat+	1	20.00%	2.44%
			Vgat-	1	20.00%	2.44%
Stellate	5	12.20%	Random	4	80.00%	9.76%
			Vgat+	1	20.00%	2.44%
			Vgat-	0	0.00%	0.00%
Narrow-field	5	12.20%	Random	4	80.00%	9.76%
			Vgat+	0	0.00%	0.00%
			Vgat-	1	20.00%	2.44%
Wide-field	7	17.07%	Random	4	57.14%	9.76%
			Vgat+	3	42.86%	7.32%
			Vgat-	0	0.00%	0.00%

Genotype		100.00%	Morphology	41	300.00%	
	41	41		41	41	100.00%
Random	28	68.29%	Unidentified	13	46.43%	31.71%
			Horizontal	3	10.71%	7.32%
			Stellate	4	14.29%	9.76%
			Narrow-field	4	14.29%	9.76%
			Wide-field	4	14.29%	9.76%
Vgat+	11	26.83%	Unidentified	6	54.55%	14.63%
			Horizontal	1	9.09%	2.44%
			Stellate	1	9.09%	2.44%
			Narrow-field	0	0.00%	0.00%
			Wide-field	3	27.27%	7.32%
Vgat-	2	4.88%	Unidentified	0	0.00%	0.00%
			Horizontal	1	50.00%	2.44%
			Stellate	0	0.00%	0.00%
			Narrow-field	1	50.00%	2.44%
			Wide-field	0	0.00%	0.00%

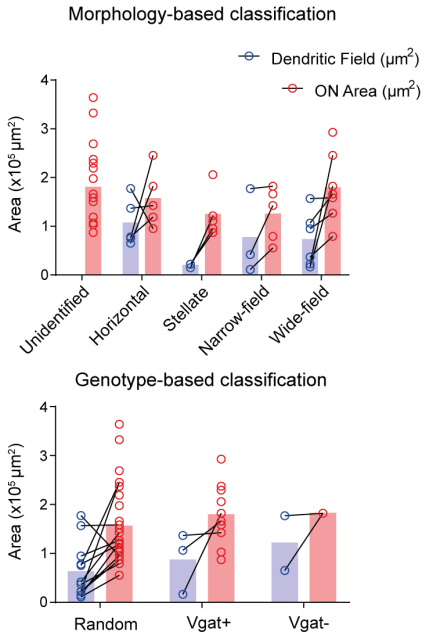

Fig. S4: Identification of SCs cell types used for electrophysiology analysis

(a) Reconstructed morphologies from various subtypes of SCs neurons that were recorded and presented in Fig. 1, including wide-field, narrow-field, stellate and horizontal neurons, that were stained with Neurobiotin.

(b-c) Quantification and classification of cell types according to morphology (i.e. horizontal, stellate, etc.) and genotype (i.e. vGAT+/- or random type). A total of n = 41 were performed of which a subset of n = 24 were included in the analysis shown in Fig. 1.

(d) Relationship between dendritic field and the neuron's corresponding retinorecipient center zone. Individual center (C) zones typically exceed the area of the dendritic zone. Note that this correlation was performed for recorded neurons where morphological data were successfully obtained.

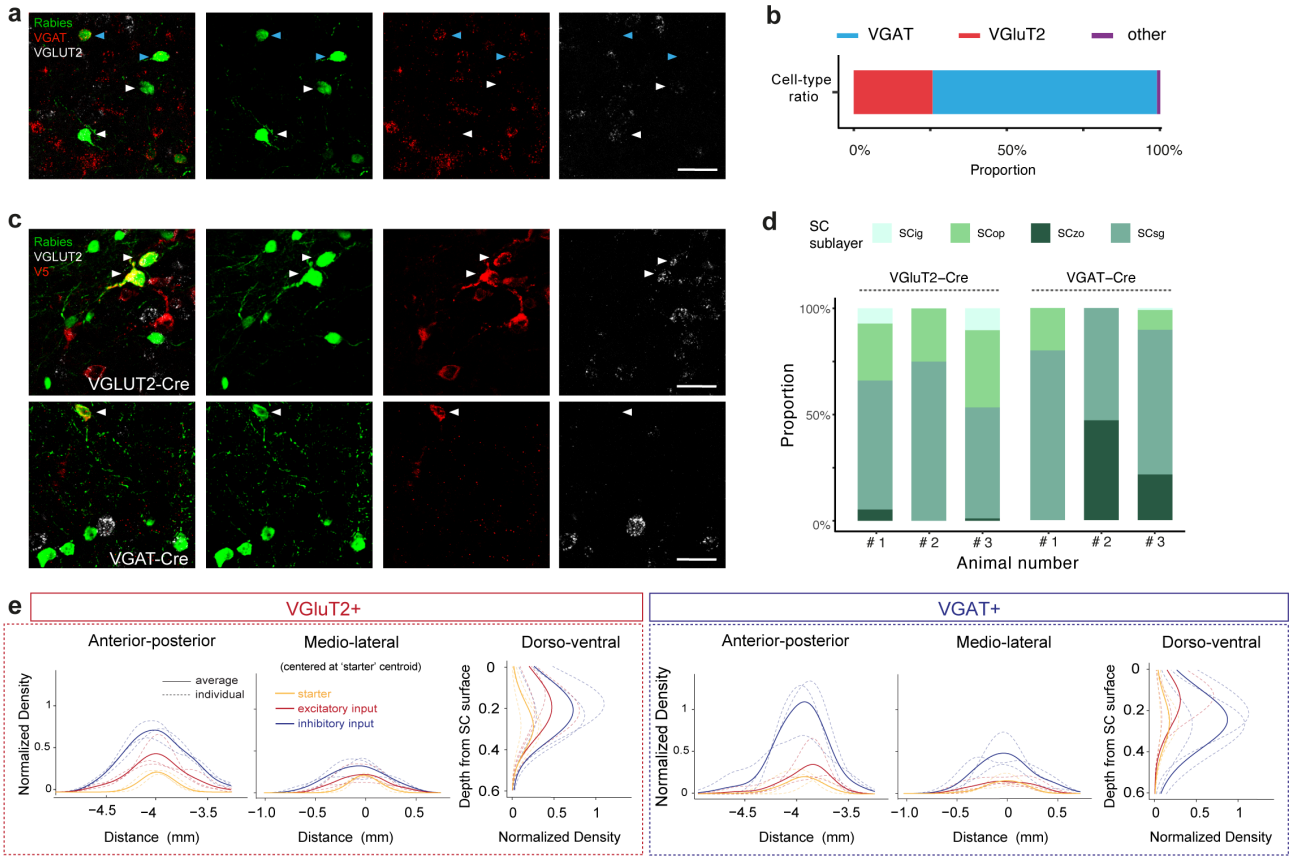

Fig. S5: Classification of vGluT2 and vGAT cell types and their distribution across the SCs. **(a)** Coexpression of vGAT and vGluT2 *in situ* hybridization in the SCs using RNAscope ISH performed to reveal the identity of input neurons. White arrows indicate Rb-EGFP+ cells that are positive for vGluT2 and negative for vGAT, suggesting that these input neurons are excitatory. By contrast blue arrows show Rb-EGFP+ cells that are inhibitory since they are positive for vGAT and negative for vGluT2. Scale bar: 25 µm.

(b) The proportion of vGluT2+ (red, n = 70) and vGAT+ (blue, n = 199) input cells that colocalize with Rb-EGFP. Unidentified neurons shown in gray (n = 3/272). N = 1 animal for each group, 3 sections were used per animal. Total number of counted neurons is: 272.

(c) RNAscope ISH for identity confirmation of starter neurons (*see* white arrows). Top row: Colocalization of vGlut2 detected in cells that express Rb-EGFP and the Cre-inducible V5 tag expressed in vGluT2-Cre mouse line, confirm starter neurons are excitatory. Bottom row: The same approach applied in a vGAT-Cre. Colocalization Rb-EGFP+ with V5+ but negative for vGluT2, suggests that the starter neuron is putatively inhibitory. Scale bar: 25 µm.

(d) the distribution of starter neurons in each animal, shown as proportion in different sublayers. The cell count for starter neurons of each animal are: vGLUT2 #1: 52; #2: 16; #3: 79. vGAT #1: 5; #2: 17; #3: 106.) SCig: SC, motor related, intermediate gray layer, SCop: superior colliculus, optic layer, SCsg: SC, superficial gray layer; SCzo: SC, zonal layer.

(e) Normalized density plot of starter and input neurons along anterior-posterior axis (AP; Left), medio-lateral axis (ML; Center) or depth from SC surface (Right). Distribution of excitatory and inhibitory neurons are shown in the top and bottom rows, respectively. The ML density plot is computed on the relative coordinates to the k-means centroid of starter cells. Dashed lines represent individual animals and solid lines show the average.

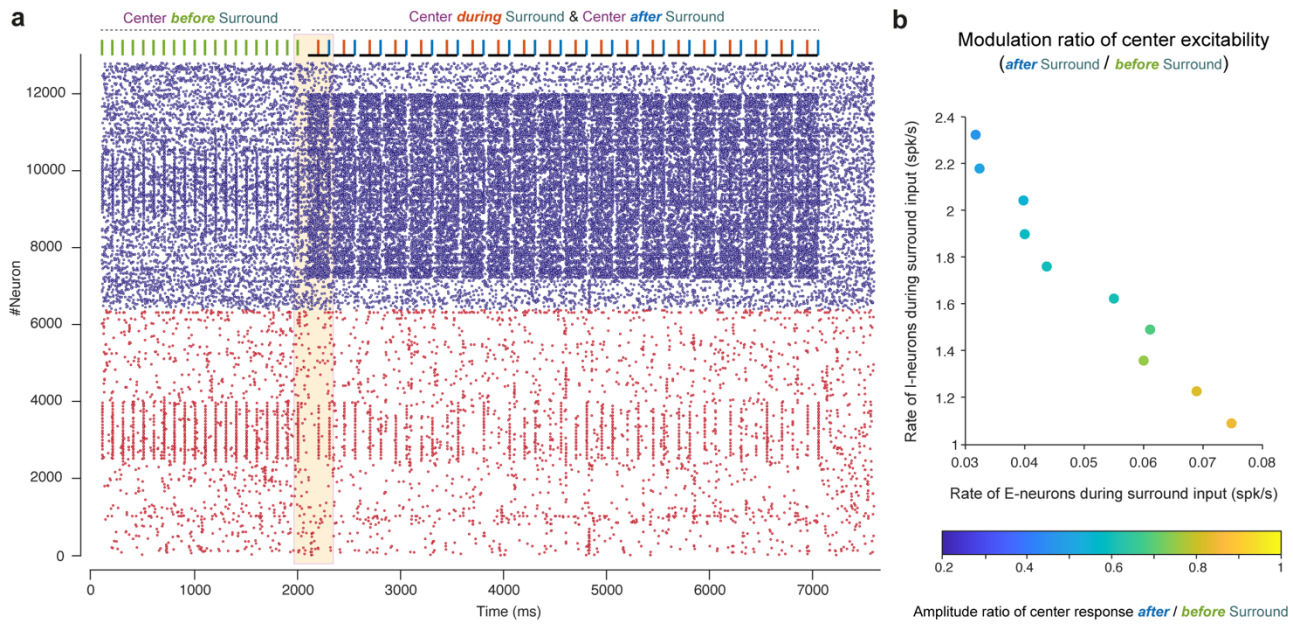

Fig. S6 Complete raster of spiking network simulation (supplemental to Fig. 3b)
(a) Entire time course of network simulation illustrating the raster of spiking activity of excitatory (red dots) and inhibitory SCs neurons (blue points) during the four stimulus conditions shown in Fig. 3. Vertical green lines show the time onset of 'center *only'* stimulation; black horizontal lines show 'surround' stimulation; vertical red and blue lines indicate the time onset of 'center *during* surround' and 'center *after* surround'. A sub-region of this trial containing all simulation conditions has been selected (orange shaded region) and shown in Fig. 3b-c.
(b) Spiking frequency of model inhibitory neurons as a function of the spiking frequency of excitatory neurons. The inverse relationship is correlated of the peak amplitude ratio of the 'center *after* surround' divided by the 'center *before* surround' response (*see* color map).

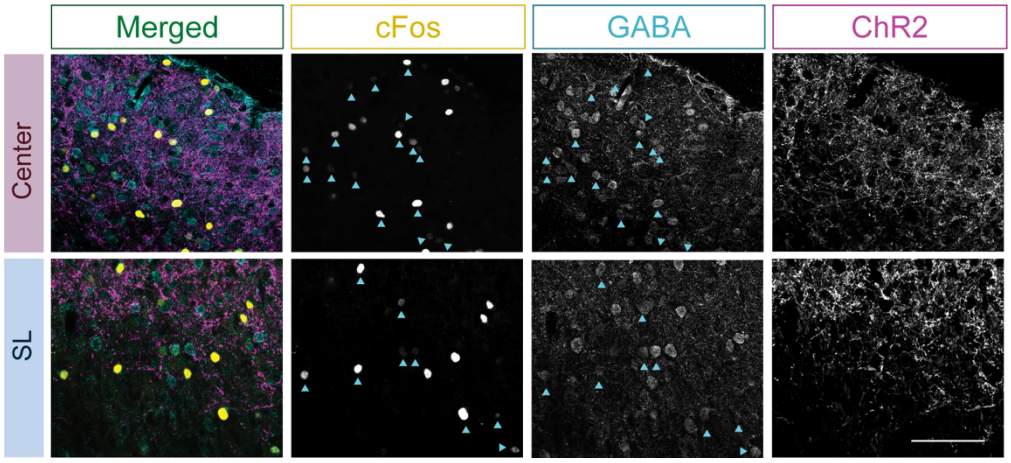

Fig. S7: Functional shifts in surround network E/I balance (supplemental to Fig. 4d)
In vivo cFos expression resulting from local optostimulaon of RGC axonal terminals in two regions of interest: 1) center zone defined as the area under the tip of the optic fiber implanted in the SCs (top row), and 2) lateral zone relative to the center referred to as 'surround lateral' (SL; bottom row). From left to right columns: a) merged image, b) *c*Fos staining, c) GABA immunostaining (arrows show colocalization), and d) ChR2-expressing retinal ganglion axonal terminals. ChR2 shown in magenta; *c*Fos in yellow; GABA in cyan. A higher ratio of active inhibitory neurons is found to be engaged in the surround after center zone stimulation (*see* Fig. 4d). Scale bar is 50 µm.